Geosci. Model Dev. Discuss., 8, 8063–8116, 2015
www.geosci-model-dev-discuss.net/8/8063/2015/
doi:10.5194/gmdd-8-8063-2015

Geoscientific Model Development Discussions
Open Access

The carbon cycle in the Australian Community Climate and Earth System Simulator (ACCESS-ESM1) – Part 1: Model description and pre-industrial simulation

R. M. Law[1], T. Ziehn[1], R. J. Matear[2], A. Lenton[2], M. A. Chamberlain[2], L. E. Stevens[1], Y. P. Wang[1], J. Srbinovsky[1], D. Bi[1], H. Yan[1], and P. F. Vohralik[3]

[1]CSIRO Oceans and Atmosphere, PMB 1, Aspendale, Victoria, Australia
[2]CSIRO Oceans and Atmosphere, Hobart, Tasmania, Australia
[3]CSIRO Manufacturing, Lindfield, New South Wales, Australia

Received: 30 June 2015 – Accepted: 30 August 2015 – Published: 18 September 2015

Correspondence to: R. M. Law (rachel.law@csiro.au)

Published by Copernicus Publications on behalf of the European Geosciences Union.

Abstract

Earth System Models (ESMs) that incorporate carbon-climate feedbacks represent the present state of the art in climate modelling. Here, we describe the Australian Community Climate and Earth System Simulator (ACCESS)-ESM1 that combines existing ocean and land carbon models into the physical climate model to simulate exchanges of carbon between the land, atmosphere and ocean. The land carbon model can optionally include both nitrogen and phosphorous limitation on the land carbon uptake. The ocean carbon model simulates the evolution of nitrate, oxygen, dissolved inorganic carbon, alkalinity and iron with one class of phytoplankton and zooplankton. From two multi-centennial simulations of the pre-industrial period with different land carbon model configurations, we evaluate the equilibration of the carbon cycle and present the spatial and temporal variability in key carbon exchanges. For the land carbon cycle, leaf area index is simulated reasonably, and seasonal carbon exchange is well represented. Interannual variations of land carbon exchange are relatively large, driven by variability in precipitation and temperature. We find that the response of the ocean carbon cycle shows reasonable agreement with observations and very good agreement with existing Coupled Model Intercomparison Project (CMIP5) models. While our model over estimates surface nitrate values, the primary productivity agrees well with observations. Our analysis highlights some deficiencies inherent in the carbon models and where the carbon simulation is negatively impacted by known biases in the underlying physical model. We conclude the study with a brief discussion of key developments required to further improve the realism of our model simulation.

1 Introduction

Over recent decades many climate models have evolved into earth system models (ESMs), a term used to identify models that simulate biogeochemical cycles and their interaction with human and climate systems. Of principal concern is the carbon cycle.

GMDD
8, 8063–8116, 2015

Anthropogenic emissions of carbon lead to increased concentrations of atmospheric carbon dioxide (CO_2). This directly impacts uptake of carbon by the land and ocean systems and warms the climate. Climate warming, in turn, perturbs the carbon uptake, typically leading to reduced carbon uptake and a positive feedback on warming. This climate-carbon feedback was first explored by Cox et al. (2000) and Friedlingstein et al. (2001) and compared across models in Friedlingstein et al. (2006). This model intercomparison confirmed that all models gave a positive carbon-climate feedback but the magnitude of that feedback was very variable across models.

The Coupled Model Intercomparison Project (CMIP5) (Taylor et al., 2012) included additional model output and extra model simulations for those models that could simulate the carbon cycle. Evaluations were conducted of the model simulated carbon fluxes over the historical period (Anav et al., 2013) and the relationship of land carbon fluxes to different climate variables (Shao et al., 2013). Future carbon fluxes were compared across models for simulations with prescribed atmospheric CO_2 (Jones et al., 2013) and emissions-driven simulations (Friedlingstein et al., 2014). The range of results for the emissions-driven simulations was similar to that found by Friedlingstein et al. (2006) with the main cause of the large range being differences in the land carbon cycle projections. Feedback analysis was conducted by Boer and Arora (2012) and Arora et al. (2013).

The Australian Community Climate and Earth System Simulator, ACCESS, has been developed over recent years to meet both the numerical weather prediction (Puri et al., 2013) and climate simulation needs (Bi et al., 2013b) of the Australian Bureau of Meteorology, CSIRO and Australian university researchers. For climate needs, the initial aim was to put together a physical coupled climate model for participation in CMIP5. A second aim is to add the carbon cycle and implement an atmospheric chemistry scheme. Two versions of ACCESS participated in CMIP5 (Dix et al., 2013), ACCESS1.0 and ACCESS1.3 (Bi et al., 2013b), differing in their atmosphere model settings and land surface scheme. Development of the earth system version of ACCESS is based on ACCESS1.4, an updated version of ACCESS1.3 (Fig. 1). This paper documents the ad-

GMDD
8, 8063–8116, 2015

dition of the carbon components to ACCESS, to give the ESM configuration, ACCESS-ESM1 as well as noting the physical model differences between ACCESS1.3 and ACCESS1.4. Model inputs required to run CMIP5-type carbon simulations are presented, along with analysis of the behaviour of the ACCESS-ESM1 model under pre-industrial conditions and prescribed atmospheric CO_2. In particular, we focus our presentation on showing and assessing the carbon flows in the land and the carbon exchanges between the land, atmosphere and ocean. A companion paper, Ziehn et al. (2015) evaluates simulations covering the historical period (1850–2005), while simulations for future periods (2005–2100) and emissions-driven simulations will be presented elsewhere.

2 ACCESS-ESM1 model description

ACCESS-ESM1 comprises the ACCESS1.4 physical climate model (Sect. 2.1), with new capability to simulate the carbon cycle. Land carbon fluxes (Sect. 2.2) are simulated as part of the Community Atmosphere Biosphere Land Exchange (CABLE) model which includes a module to simulate carbon exchange between land carbon pools, with the optional inclusion of nutrient limitation. Ocean carbon fluxes (Sect. 2.3) are simulated by the World Ocean Model of Biogeochemistry And Trophic-dynamics (WOMBAT). Versions of CABLE and WOMBAT have been documented previously (e.g., Kowalczyk et al., 2006; Oke et al., 2013). Hence the descriptions below are mostly limited to any model developments since the earlier work and specifics of the model implementation in the ACCESS-ESM1 context. The focus is on the carbon fluxes from the land and ocean that are input to the atmosphere (Sect. 2.4), either actively influencing climate through the atmospheric CO_2 field or as passive tracers for comparison with observed atmospheric CO_2.

GMDD
8, 8063–8116, 2015

2.1 Physical model: ACCESS1.4 compared to ACCESS1.3

As described in Bi et al. (2013b) and illustrated in Fig. 1, the atmospheric component of ACCESS1.3 is the UK Met Office Unified Model (UM) (Martin et al., 2010; The HadGEM2 Development Team, 2011) to which the land surface model, CABLE, is directly coupled; the ocean component is a version of the NOAA/GFDL Modular Ocean Model (MOM4p1) (Griffies, 2009) and sea-ice is modelled using the LANL CICE4.1 model (Hunke and Lipscomb, 2010) with coupling of the ocean and sea-ice to the atmosphere with the OASIS coupler (Valcke, 2013). The ACCESS configuration of the ocean and sea-ice components, ACCESS-OM, is described in Bi et al. (2013a) with CMIP5 evaluations documented in Marsland et al. (2013) and Uotila et al. (2013). The ocean-only configuration of ACCESS has been extensively used to explore intrinsic variability in the ocean and the role it may play in decadal variability (e.g. O'Kane et al., 2013).

The physical model to which we are adding the carbon cycle is derived from ACCESS1.3 and designated ACCESS1.4. ACCESS1.4 addresses a number of issues that were identified during the analysis of the ACCESS1.3 CMIP5 simulations and also includes an updated version of CABLE (CABLE2). Changes made to CABLE are discussed in Sect. 2.2. Details of other changes between ACCESS1.3 and ACCESS1.4 are documented here.

2.1.1 Atmosphere component

ACCESS1.3 used atmospheric physics settings similar to the Met Office Global Atmosphere (GA) 1.0 configuration (Hewitt et al., 2011) including the "PC2" cloud scheme (Wilson et al., 2008). A similar configuration is used for ACCESS1.4.

Analysis of ACCESS1.3 simulations showed almost no dust in the atmosphere (Dix et al., 2013); this was a consequence of changing the land surface scheme from the original UM land scheme to CABLE and freezing the ACCESS1.3 code version for CMIP5 before finalising dust settings. As described in Dix et al. (2013), the dust-uplift

GMDD
8, 8063–8116, 2015

scheme used in the ACCESS models is based on Woodward (2001) and Woodward (2011), with dust being modelled for nine size bins with different particle diameters. Dust uplift can occur over bare soil and depends on wind speed, soil composition and volumetric soil-moisture content in the surface layer. Dust-uplift settings used by ACCESS1.4 for the tuneable parameters described in Woodward (2011) are friction-velocity tuneable constant $k_1 = 1.6$, soil-moisture tuneable constant $k_2 = 0.5$, overall scaling factor $C = 6.525$, maximum clay fraction for dust emissions of 0.1 and no preferential source term. These settings result in a global annual mean dust burden of 14.9 ± 1.3 Tg (calculated over 160 years from an ACCESS1.4 pre-industrial control simulation), which is broadly comparable to the AEROCOM multi-model median value of 15.8 Tg for year 2000 conditions (Huneeus et al., 2011).

In addition to the change in dust, the ACCESS1.3 control simulation did not include background stratospheric volcanic forcing but this has been included in ACCESS1.4 simulations. Preliminary tests with the dust and vocanic forcing changes reduced the globally averaged surface air temperature relative to ACCESS1.3. Since an aim of ACCESS1.4 was not to change global-scale climate characteristics relative to ACCESS1.3, one of the parameters in the cloud scheme (FW_STD associated with the standard deviation of cloud water content) was increased from 0.700 in ACCESS1.3 to 0.725 in ACCESS1.4. This resulted in a globally averaged surface air temperature in ACCESS1.4 that was similar to that obtained for ACCESS1.3. ACCESS1.4 also corrects a bug which zeroed the downward short-wave radiation over coastal sea-ice points for non-radiation timesteps. This reduced excess ice accumulation in ACCESS1.3 in some coastal regions such as the Canadian Archipelagos.

2.1.2 Ocean component

While there are no changes in the ocean model version between ACCESS1.3 and ACCESS1.4, there have been two changes in the configuration or parameter values. Firstly for ACCESS1.4, the background vertical diffusivity outside 20° S to 20° N has been increased from 0.5×10^{-5} to 1.0×10^{-5} $m^2 s^{-1}$, which is also consistent with the

GMDD
8, 8063–8116, 2015

value used in ACCESS-OM. Secondly, the ocean absorption of penetrative solar radiation is now calculated using the diffuse attenuation coefficient of the downwelling photosynthetically available radiation (K_{dPAR}) rather than the downwelling spectral irradiance at wavelength 490 nm (K_{d490}). Since K_{dPAR} data covers a broader, more representative, spectrum of light, it is considered to be more appropriate for use in the ocean model and was also the dataset used in the standard ACCESS-OM configuration. Bi et al. (2013a) compares ACCESS-OM simulations using K_{dPAR} and K_{d490} and concludes that differences are mostly confined to the subsurface water between 40° S to 40° N with little impact on the deep ocean climate or the global ocean circulation and associated water volume transports.

2.1.3 OASIS coupler

ACCESS1.3 used the OASIS3.2-5 coupler (Valcke, 2006). In ACCESS1.4, this is replaced by OASIS3-MCT (Valcke et al., 2013) which is designed to provide more efficient coupling for models running on many processors. For ACCESS1.4, this enables the simulation of about 7.2 model years per day (using 144 processors) compared to 5.4 model years per day for ACCESS1.3.

2.2 Land carbon model: CABLE

CABLE is a land surface model that simulates the fluxes of momentum, heat, water and carbon across the land-atmosphere interface. CABLE operates both in standalone mode (forced with prescribed meteorology) and coupled to atmospheric models (at least five different models to date, both global and regional). The history and scientific core of CABLE version 1 is most fully described in Kowalczyk et al. (2006) with a summary description provided in the Appendix of Wang et al. (2011). CABLE was initially implemented in ACCESS1.3 at version 1.8 (CABLE1.8, Kowalczyk et al., 2013). CABLE version 2 was designed to provide a consolidation of the standalone and ACCESS versions of CABLE into a single code repository with common science routines.

GMDD
8, 8063–8116, 2015

In particular, this enabled the ACCESS version to optionally run with a biogeochemical module (Wang et al., 2010), which was initially developed for the standalone version.

ACCESS1.4 and ACCESS-ESM1 use CABLE2.2.3 (Fig. 1), but in ACCESS1.4 the biogeochemical module is not switched on. Apart from the inclusion of the biogeochemical module, CABLE2.2.3 has a number of small science changes and bug fixes from CABLE1.8 (used in ACCESS1.3). These dealt with occasional non-physical exchange coefficients, addressed some poor behaviour under very dry conditions, improved the water balance in the coupled system and ensured all CABLE variables were correctly being passed back into the ACCESS atmosphere e.g. for use by dry deposition. Often these changes could be shown to improve CABLE's performance in standalone mode for individual locations (e.g. at desert sites for the dry condition changes) but did not have broad-scale impacts when tested globally in atmosphere-only ACCESS simulations. Thus the assessment of the land surface impacts on the ACCESS climate for ACCESS1.3 (Kowalczyk et al., 2013) would also be applicable to ACCESS1.4 and ACCESS-ESM1 simulations. The improvements to the water balance approximately halved the drift in global ocean salinity in ACCESS1.4 compared to ACCESS1.3.

In ACCESS, CABLE is run for one or more tiles in each grid-cell with a non-zero land fraction. Each tile represents a different vegetated or non-vegetated surface type with a number of CABLE input parameters being surface type dependent (Sect. 3.1.1). Each tile is modelled with a separate soil column beneath the surface. The biogeochemistry module, denoted CASA-CNP, simulates the flow of carbon, and optionally, nitrogen and phosphorus between three plant biomass pools (leaf, wood, roots), three litter pools (metabolic, structural, coarse woody debris) and three organic soil pools (microbial, slow, passive), one inorganic soil mineral nitrogen pool and three other phosphorus pools (labile, sorbed, strongly sorbed).

The flux of carbon from the land to the atmosphere has two components, net ecosystem exchange (NEE) and fluxes due to disturbance (e.g. fire) and land-use change. Currently CABLE simulates the former, as the difference between respiration and pho-

GMDD
8, 8063–8116, 2015

tosynthesis, but not the latter. Thus

$$\mathrm{NEE} = -1 \times \mathrm{NEP} \quad (1)$$

and net ecosystem production (NEP) is the difference between gross primary production (GPP) and plant (or autotrophic, R_a) and soil (or heterotrophic, R_h) respiration

$$\mathrm{NEP} = \mathrm{GPP} - R_a - R_h = \mathrm{NPP} - R_h \quad (2)$$

where NPP is net primary production.

GPP and leaf maintenance respiration are calculated every time step using a two-leaf (sunlit and shaded) canopy scheme (Wang and Leuning, 1998).

$$\mathrm{GPP} = f(\mathrm{LAI}, v_{\mathrm{cmax}}, j_{\mathrm{max}}) \quad (3)$$

where LAI is leaf area index, v_{cmax} is the maximum rate of carboxylation and j_{max} is the maximum rate of potential electron transport. LAI may be prescribed or simulated, with simulated (prognostic) LAI being dependent on the size of the leaf carbon pool (c_{leaf}) and the specific leaf area (SLA), which is a vegetation dependent parameter:

$$\mathrm{LAI} = \max(\mathrm{LAI}_{\mathrm{min}}, c_{\mathrm{leaf}} \times \mathrm{SLA}) \quad (4)$$

where the max function ensures a vegetation dependent minimum LAI ($\mathrm{LAI}_{\mathrm{min}}$). Section 4.2.1 notes an unintended impact of this minimum LAI constraint. v_{cmax} and j_{max} are vegetation dependent parameters for carbon only simulations, but when nutrient limitation is active, v_{cmax} and j_{max} become dependent on leaf nitrogen (n_{leaf}) and phosphorus to nitrogen ratio (p_n) (Zhang et al., 2013; Wang et al., 2012):

$$v_{\mathrm{cmax}} = a + bf(p_n)n_{\mathrm{leaf}} \quad (5)$$

$$j_{\mathrm{max}} = 2v_{\mathrm{cmax}} \quad (6)$$

GMDD
8, 8063–8116, 2015

where a and b are vegetation type dependent empirical coefficients taken from Kattge et al. (2009) (Supplement, Table S1). For evergreen broadleaf forest $f(p_n)$ is expressed as:

$$f(p_n) = 0.4 + 9p_n \quad (7)$$

and set to one for other vegetation types due to the lack of data (Zhang et al., 2013).

Daily mean GPP and leaf respiration are passed into the biogeochemical module which is run once per day to calculate the remaining respiration fluxes and the carbon flow between pools. The fractions of GPP allocated to each vegetation pool are vegetation dependent parameters which, for non-evergreen vegetation types, are also dependent on leaf phenology phase (Wang et al., 2010). The phenology phase is prescribed by latitude and vegetation type and is based on remote sensing data (Zhang et al., 2004, 2005).

Maintenance respiration of woody tissue and roots and growth respiration are calculated as a function of mean daily air temperature and tissue nitrogen amount. Default carbon to nitrogen and nitrogen to phosphorus ratios are used when nitrogen and/or phosphorus are not simulated. Growth respiration is calculated daily as a proportion of the difference between daily GPP and plant maintenance respiration, with the proportion being a function of leaf nitrogen to phosphorus ratio (Zhang et al., 2013). Microbial respiration from decomposition of litter and soil carbon is also calculated daily and depends on the amount of organic carbon (or substrate quantity), the nitrogen to carbon ratio of organic carbon in litter or soil (substrate quality), and soil temperature and moisture (Kelly et al., 2000). We used a Q10-type function to describe the dependence of microbial respiration on soil temperature, although other functions can also be used (Exbrayat et al., 2013).

Since plant and soil respiration rates are only calculated daily, CABLE in ACCESS-ESM1 is not expected to realistically simulate the diurnal cycle of the net land carbon flux to the atmosphere, and we restrict our analysis to monthly or longer timescales.

GMDD
8, 8063–8116, 2015

Carbon should be conserved across the land carbon system, that is the net flux to the atmosphere over a given time period should equal the change in the total carbon across all carbon pools over that same period. A carbon conservation check is presented in Sect. 4.2.1.

CABLE with CASA-CNP has been used in a number of offline applications, where meteorological forcing is prescribed, (e.g., Huang et al., 2015) as well as in a low resolution earth system model in atmosphere-only simulations (Zhang et al., 2011, 2013; Wang et al., 2015) or in atmosphere-ocean coupled simulations (Zhang et al., 2014). Experience from these studies has guided configuration and parameter choices for CABLE in ACCESS-ESM1 (Sect. 3).

2.3 Ocean carbon model: WOMBAT

The Whole Ocean Model of Biogeochemistry And Trophic-dynamics (WOMBAT) model is based on a NPZD (Nutrient, Phytoplankton, Zooplankton and Detritus) model with the additions of bio-available iron limitation (Fe), dissolved inorganic carbon (DIC), calcium carbonate ($CaCO_3$), alkalinity (ALK), and oxygen (O). At present WOMBAT includes only one class each of phytoplankton and zooplankton. All biogeochemical (BGC) tracers are calculated on the same grid as temperature. The equations of WOMBAT are given in Oke et al. (2013, Appendix B) and the parameters used in this simulation are given in Table 1. In our simulations our nutrient is phosphate and hence we do not explicitly simulate nitrate. In our later comparisons we convert phosphate to nitrate using the stoichiometric ratios of Anderson and Sarmiento (1994).

In this model we include two DIC tracers: natural and anthropogenic DIC. These two DIC tracers only differ in the atmospheric CO_2 concentration used in the air–sea flux calculation. For the natural DIC, the atmospheric CO_2 was kept at 285 ppm while for anthropogenic DIC the atmospheric CO_2 increases according to the historical or future atmosphere concentration. At the surface we calculate the air–sea exchange of the two carbon tracers and oxygen following Lenton and Matear (2007), which uses the difference in partial pressure between the ocean and atmosphere, the simulated

GMDD
8, 8063–8116, 2015

sea-ice concentrations, and the wind-speed squared and temperature dependent gas exchange coefficient following Wanninkhof (1992). WOMBAT simulates the biological production and export of particulate organic carbon (detritus) and calcium carbonate from the photic zone and its subsequent remineralization in the ocean interior. The remineralization of particulate organic matter occurs through prescribed remineralization and sinking rates. The model maintains particulate organic matter and calcium carbon sediment pools so that any particulate material reaching the sediments is remineralized back into the overlying water at the same remineralization rate as the water column values. The sediment pools are included to improve numerical stability of the ocean carbon module by preventing the instantaneous remineralization of particulate material in the deepest layer of the model.

2.4 Atmospheric carbon dioxide

ACCESS-ESM1, mostly through capability inherited from the Met Office Unified Model, has the option of running with or without interactive CO_2. When interactive CO_2 is selected, a three-dimensional atmospheric CO_2 field is simulated and atmospheric CO_2 is transported through the atmosphere. This CO_2 field influences the radiation calculation in the model as well as the calculation of the land and ocean carbon fluxes through CABLE and WOMBAT respectively. The atmospheric CO_2 field is, in turn, dependent on the land and ocean carbon fluxes into or out of the atmosphere, along with any additional prescribed (e.g. anthropogenic) carbon flux. In this mode, ACCESS-ESM1 can simulate any climate-carbon feedback that might result from increasing anthropogenic carbon fluxes. This mode is used for the CMIP5 "emissions-driven" simulations. While maintaining an interactive 3-D CO_2 field, an additional switch in ACCESS-ESM1, allows the model radiation scheme to revert to responding to a prescribed (usually spatially constant) atmospheric CO_2 mixing ratio. This enables simulations to be run that separate the direct effects of increasing atmospheric CO_2 on simulated carbon fluxes from how the climate affects carbon fluxes.

GMDD
8, 8063–8116, 2015

When ACCESS-ESM1 is run without interactive CO_2, the radiation scheme and carbon flux models are forced with a common prescribed atmospheric CO_2 concentration. This might be constant in time for a pre-industrial control run, or increasing in time for historical or future scenarios. Many of the CMIP5 simulations run in this mode. When running in this way, we have also enabled the model to pass the land and ocean carbon fluxes into two of the passive tracer fields that are part of the Unified Model code. These tracers are transported through the atmosphere and allow us to assess the separate contributions of land and ocean carbon fluxes to features in observed atmospheric CO_2 such as the seasonal cycle or interannual variability.

The atmospheric transport of CO_2 does not perfectly conserve carbon. To ensure that carbon is conserved in the atmosphere, a mass fixer has been applied as described in Sect. 2.2.2 of Jones et al. (2011).

3 Model configuration

The ACCESS-ESM1 atmosphere is run with a horizontal resolution of 1.875° longitude × 1.25° latitude, and with 38 vertical levels. The ocean horizontal resolution is nominally 1°, with latitudinal refinements around the equator (0.33 between 10° S and 10° N) and the Southern Ocean (ranging from 0.25 at 78° S to 1° at 30° S), and a tripolar Arctic north of 65° N (Bi et al., 2013a).

As noted above, CABLE can simulate land carbon fluxes with or without nutrient limitation. Here we have chosen to run CABLE in the "CNP" configuration, based on results from some low resolution ESM studies. Zhang et al. (2014) assessed the sensitivity of allowable emissions to nutrient limitation comparing cases running the carbon cycle alone (C), carbon and nitrogen (CN) or carbon, nitrogen and phosphorus (CNP). Depending on the scenario and time period considered, the CN case reduced land carbon uptake by 35–40 % relative to the C case, with a further 20–30 % reduction in the CNP case. The CN and CNP cases were within the uncertainty range of observed land carbon uptake for the historical period. Zhang et al. (2013) assessed the interaction

GMDD
8, 8063–8116, 2015

of land cover change with nutrient limitation. Again the CNP case gave land carbon uptake more consistent with observations than the C only case.

For most of the work described here, two sets of simulations have been performed. In the first set, leaf area index is prescribed and there should be no interaction between the carbon cycle and the climate simulation (given that atmospheric CO_2 is prescribed in these simulations). In the second set, LAI is prognostic and dependent on the size of the leaf carbon pool. In this case, the change in LAI has an impact on climate through its influence on radiation absorption and momentum, heat and moisture fluxes. The climate impact will be briefly examined in Sect. 4.1. The ocean carbon model configuration was the same for both the prescribed LAI and prognostic LAI simulations.

3.1 Input files

3.1.1 Land

Most of the input files and parameter settings (Supplement) for the biophysical component of CABLE were as described in Kowalczyk et al. (2013) including the LAI used in our prescribed LAI simulation. Note that the same LAI is used for all vegetation types within a grid-cell.

Differences between the model configuration here and Kowalczyk et al. (2013) are (a) a slight difference in the vegetation distribution used and (b) a change in the leaf optical property parameters. Thirteen surface types are differentiated: four forest types (evergreen needleleaf, evergreen broadleaf, deciduous needleleaf, deciduous broadleaf), six shrub and grass types (shrub, C3 grass, C4 grass, tundra, crop, wetland) and three non-vegetated types (lakes, ice, bare ground). As in Kowalczyk et al. (2013) the vegetation distribution is derived from Lawrence et al. (2012) but where Kowalczyk et al. (2013) restricted each grid-cell to three dominant vegetation types, here vegetation types are selected based on whether they ever occur at greater than 10 % of the grid-cell at any time between 1850 and 2100 (under any CMIP5 RCP scenario). While the simulations presented here do not account for land-use change and

GMDD
8, 8063–8116, 2015

are all run with a pre-industrial (1850) vegetation distribution, the vegetation dataset has been constructed to allow further simulations in which the impacts of land-use change are modelled. The vegetation distribution includes a small number of wetland tiles but due to an incorrect setting for CASA-CNP, these were effectively excluded from the simulation of carbon fluxes. The small area involved means there is no significant impact on any simulation results presented here. The change in leaf optical properties (reflectance and transmission) for ACCESS-ESM1 was designed to be more consistent with the snow-free soil albedo used in ACCESS. The change was made to improve the low albedo simulated by ACCESS1.3 (Kowalczyk et al., 2013).

Additional input files are required for the biogeochemistry module of CABLE and these are based on Wang et al. (2010). Parameters (Supplement) such as the fraction of NPP allocated to different pools and turnover times are specific to each vegetation type and are set from literature values or tuned based on offline simulations (Wang et al., 2010). We use the same prescribed leaf phenology as Wang et al. (2010) which gives the timing of green-up and leaf fall by latitude for all vegetation types except evergreen trees. We note here the limitation of using present day leaf phenology for pre-industrial simulations and the inability of the model to simulate a changing growing season with changing climate.

To simulate nitrogen and phosphorus requires nitrogen deposition and fixation, phosphorus from weathering and from dust and soil order, to distinguish soils of different mineralogy and age. These are all taken from Wang et al. (2010), re-gridded for the ACCESS-ESM1 model resolution and are representative of present-day conditions with no temporal variation. Nitrogen and phosphorus fertiliser application rates are also taken from Wang et al. (2010) and applied to all crop tiles (in the 1850 vegetation distribution used here).

3.1.2 Ocean

The initial conditions for phosphate (P) and oxygen (O_2) are derived from the 2005 version of the World Ocean Atlas (WOA2005; Garcia et al., 2006a, b). Phytoplankton

GMDD
8, 8063–8116, 2015

in the top 100 m was initialised using Chlorophyll (Chl *a*) taken from a climatology of SeaWIFS (1997–2008) and then scaled to Phosphorus units using the ratio P : Chl *a* = 1/16 mmol m^{-3} P : 1.59 mg m^{-3} Chl *a*. Zooplankton was initialised as 0.05 of the initial phytoplankton concentrations. The initial field for Iron (Fe) was taken from a 500 year integration of a coarser resolution simulation of WOMBAT. Pre-industrial DIC and ALK are initialised from the Global Ocean Data Analysis Project (GLODAP, Key et al., 2004).

3.2 Spin-up

There was no formal spin-up of the carbon cycle before the ACCESS-ESM1 pre-industrial control run was started. The land carbon pools were initialised at values taken from repeated test simulations using the prognostic LAI configuration. The ocean BGC initial fields come from the observed climatology as described in the previous section. Offline land simulations and ocean-only simulations were explored to aid in the spin-up process but neither produced a satisfactory result at the time the pre-industrial run was started. This partly reflected the significant and evolving change of the mean climatology of the land, ocean and atmosphere from the present-day state.

4 Results: pre-industrial control run

In this section results from two ACCESS-ESM1 pre-industrial control simulations will be characterised and compared. Each simulation presented here used prescribed (rather than interactive) atmospheric CO_2 set to 285 ppm. The first simulation ran CABLE with prescribed leaf area index, which we denote "PresLAI" and the second simulation ran CABLE with prognostic LAI, denoted "ProgLAI". The ocean carbon configuration was the same for both simulations, using the ocean parameter set in Table 1. Both these simulations have been run for 1000 years. For land carbon (Sect. 4.2), the analysis of the pre-industrial control run focusses on carbon conservation, equilibration, and variability, both spatially and temporally. We do not compare land carbon fluxes with obser-

GMDD
8, 8063–8116, 2015

vations as this is addressed in the assessment of the historical simulation presented in Ziehn et al. (2015). For ocean carbon (Sect. 4.3), the analysis of the pre-industrial control run focusses on the temporal evolution of global air–sea fluxes and primary productivity, and presents the mean state, and an estimate of interannual variability. The ocean carbon-cycle response is compared to observations where relevant, and with the results of CMIP5 models. The impact of the carbon fluxes on atmospheric CO_2 is included in Ziehn et al. (2015).

A brief analysis of the simulated climate is presented first (Sect. 4.1), noting primarily how the climate simulations are impacted by any carbon cycle configuration choices (e.g. prognostic LAI) and any deficiencies in the climate simulation that may cause problems for the carbon simulation.

4.1 Climate

Relative to the range of CMIP5 models, the two ACCESS submissions, ACCESS1.0 and ACCESS1.3 produced similar results when various modelled atmospheric climate variables were compared against observations (e.g. Flato et al., 2013, Fig. 9.7). Here we compare the ACCESS1.4 and ACCESS-ESM1 pre-industrial climate simulations against that of ACCESS1.3, using ACCESS1.0 to assess these relative differences. We calculate the root mean square difference (RMSD), similar to Gleckler et al. (2008), between each modelled field (F) and that modelled by ACCESS1.3 (R) for monthly mean values averaged across 100 years of each pre-industrial simulation for all longitude (i) and latitude (j) and, depending on the variable, at different pressure levels:

$$\mathrm{RMSD}^2 = \frac{1}{W}\sum_i\sum_j\sum_t w_{ijt}(F_{ijt} - R_{ijt})^2 \quad (8)$$

where t corresponds to the time dimension (12 months) and W is the sum of the weights (w_{ijt}) which, for the spatial domain, are proportional to the grid-cell area. We

GMDD
8, 8063–8116, 2015

then normalise by the ACCESS1.0 RMSD:

$$\mathrm{RMSD}_{\mathrm{norm}} = \mathrm{RMSD}_{\mathrm{model}}/\mathrm{RMSD}_{\mathrm{ACCESS1.0}} \quad (9)$$

such that a value of 1 indicates that the simulated variable is as different from ACCESS1.3 as ACCESS1.0 is from ACCESS1.3 while values smaller than 1 indicate a simulation that is closer to that of ACCESS1.3. Figure 2 shows that for a range of atmospheric variables the normalised RMSD for ACCESS1.4 is generally around 0.3–0.4 indicating that the ACCESS1.4 climate simulation is much closer to ACCESS1.3 than ACCESS1.0 is to ACCESS1.3. This would be expected given the relatively small number of science changes between ACCESS1.3 and ACCESS1.4. Likewise the ACCESS-ESM1 simulation with prescribed LAI shows similar RMS differences from ACCESS1.3, implying little or no change from the ACCESS1.4 simulation when the carbon cycle is included but the atmospheric CO_2 is prescribed. The RMS differences for ACCESS-ESM1 with prognostic LAI are generally similar or slightly larger than for the case with prescribed LAI, with the largest differences being for near surface and lower tropospheric temperature and geopotential height at 500 hPa. This confirms that changing the LAI has a small impact on the climate simulation.

For surface air temperature, the prognostic LAI case results in globally warmer temperatures ($14.59 \pm 0.11\,^{\circ}\mathrm{C}$ averaged over the final 300 years of the ProgLAI simulation compared to $14.22 \pm 0.10\,^{\circ}\mathrm{C}$ for the PresLAI case). The surface warming extends through the troposphere and is largest over northern high latitude continents (typically 1–2 °C) while over tropical forests the ProgLAI case is slightly cooler (around 0.5 °C) than the PresLAI case. The northern high latitude warming is more pronounced in winter than summer suggesting an interaction between LAI and snow. The simulated prognostic LAI is presented in Sect. 4.2.3; lower prognostic than prescribed LAI appears to result in lower temperatures and vice versa. Note that the temperature differences triggered by changes in LAI are small compared to the tropical-polar temperature gradient and seasonal cycles of temperature.

GMDD
8, 8063–8116, 2015

To provide a perspective on how the ocean dynamics changes between ACCESS1.3 and ACCESS1.4 we compare the global meridional overturning streamfunction and the annual maximum mixed layer averaged over the last 100 years of the 500 year control simulations. Global meridional overturning circulation is very similar in the two simulations (Fig. 3). One important difference is in the strength of the Antarctic Bottom Water (AABW) cell where ACCESS1.4 has a maximum strength of 8 Sv, which is about 2 Sv less than ACCESS1.3. With reduced AABW formation and the associated Southern Ocean deep cell, ACCESS1.4 is slightly warmer in the deep ocean (up to 0.2 °C by the end of the control run) than ACCESS1.3, which is more consistent with observations (Boyer et al., 2009). The maximum mixed layer depth is also very similar in the two simulations (Fig. 4). The most significant difference occurs in the high latitude Southern Ocean where ACCESS1.4 has shallower depths in the Ross and Weddell Seas and deeper depths to the north of these seas. This difference accounts for the reduced AABW formation of ACCESS1.4. ACCESS-ESM1 maximum mixed layer depth (not shown) is very similar to ACCESS1.4, as expected since both model versions share the same ocean configuration. Both these diagnostics show the ocean dynamics of ACCESS1.4 (and consequently ACCESS-ESM1) is very similar to ACCESS1.3 and we can use the previous analysis of ACCESS1.3 (Marsland et al., 2013; Uotila et al., 2013) to help interpret our ocean simulation.

Any climate model produces biases in its climate simulation when compared with observations. Some of these biases may also have implications for the simulation of the carbon cycle. Here we note two biases that impact on different components of the carbon cycle. Firstly, Kowalczyk et al. (2013) reported seasonal negative precipitation biases over India in June–August and over the Amazon in December–February for the ACCESS1.3 historical simulation. Similar biases are seen in all our ACCESS-ESM1 simulations, with implications for the sustainability of vegetation due to insufficient moisture (Sect. 4.2.1). Secondly salinity in the surface ocean has large regional biases (Bi et al., 2013b, Fig. 16), which produce surface alkalinity biases because al-

GMDD
8, 8063–8116, 2015

kalinity is strongly influenced by air–sea freshwater exchanges. These alkalinity biases will introduce biases in surface pCO_2 and air–sea flux of CO_2.

4.2 Land carbon

4.2.1 Land carbon conservation

The conservation of land carbon has been checked across a sample 100 year period of the PresLAI and ProgLAI simulations (years 601–700). The change in total carbon across all carbon pools over the 100 years was compared with the net carbon flux to the atmosphere across the same period for each vegetated tile. The distribution of this carbon imbalance varied with vegetation type but was typically highly skewed with a small number of large positive imbalances, indicating that the change in carbon across the pools was smaller than the flux of carbon to the atmosphere.

If we choose $\pm 2\,\mathrm{g\,C\,m^{-2}}$ over 100 years as indicative of good carbon conservation, then 85 % of vegetated tiles in the PresLAI simulation and 87 % of tiles in the ProgLAI simulation meet this criteria. The shrub vegetation type has the smallest proportion of tiles meeting this criteria (45–62 %) followed by deciduous broadleaf in the PresLAI case (70 %) and C3 grass in the ProgLAI case (75 %).

Tiles with poor carbon conservation are characterised by zero or very low leaf carbon and possibly other highly depleted carbon pools. The magnitude of the carbon imbalance is well correlated (greater than 0.9) with a count of the number of months with zero leaf carbon across the 100 year period. The low leaf carbon often appears to occur in regions with low rainfall. It is likely that a poor simulation of rainfall by the physical model in certain regions (e.g. India) is leading to insufficient moisture to support plant growth. Effectively the plants die, but while this may be a realistic response to insufficient rainfall, it is now apparent that CABLE is not handling this situation in a self-consistent manner. In the PresLAI case, this is likely due to a lack of coupling between the LAI and the leaf carbon pool but this can also occur in the ProgLAI case because the model has been coded to enforce a minimum allowed LAI (dependent on

GMDD
8, 8063–8116, 2015

vegetation type). Reformulating CABLE to better manage this situation is a high priority for future model development. The impact of the lack of carbon conservation on the overall model simulation will be noted where applicable in the analysis that follows (but is generally found to be small).

4.2.2 Flux equilibration

The temporal evolution of the global land carbon fluxes over the 1000 years of simulation is shown in Fig. 5. In the ProgLAI case (Fig. 5a), GPP is slightly smaller than the summed respiration fluxes, with both showing a small drift to smaller values over the first 400–500 years. Variations between consecutive 25 year periods can be 1–2 $\mathrm{Pg\,C\,yr^{-1}}$ and are similar between GPP and summed respiration. The variability is smaller in the PresLAI case (Fig. 5b) when the feedback from the prognostic LAI is not included. In the PresLAI case the summed respiration fluxes decrease in time, particularly over the first 300 years. This is to be expected since the prognostic LAI configuration had been run for several hundred years in test runs before the start of the 1000 year simulation but this was not the case for the PresLAI run. Respiration takes longer to equilibrate than GPP because of its dependence on carbon pools with longer turnover times.

Figure 5c shows the 25 year mean NEE for the two model configurations. Again, after the initial adjustment of the PresLAI case, the ProgLAI case is more variable than the PresLAI one. Neither case equilibrates to zero; over the last 500 years of the simulation the global NEE is 0.40 $\mathrm{Pg\,C\,yr^{-1}}$ for PresLAI and 0.14 $\mathrm{Pg\,C\,yr^{-1}}$ for ProgLAI. However tiles with poor carbon conservation contribute disproportionally to this global NEE. Excluding the 15 % of tiles with poor conservation, the NEE is reduced to 0.07 and 0.05 $\mathrm{Pg\,C\,yr^{-1}}$ for the PresLAI and ProgLAI cases respectively. In both cases, the evergreen broadleaf vegetation type makes the largest contribution to this remaining non-zero NEE, as its fluxes are slower to equilibrate than most other vegetation types (Fig. 6a). Broadleaf deciduous vegetation also stands out, showing a relatively large positive NEE in each 100 year period with only a slow decrease over time but typically

GMDD
8, 8063–8116, 2015

0.04 Pg C yr^{-1} of this is due to poorly conserving tiles. The tundra vegetation type gives negative NEE, getting closer to zero over time. Early test simulations showed some problems with soil nitrogen getting too low, which was particularly evident for the tundra vegetation type; tundra pools are still recovering in the first 500 years of this simulation. Evergreen needleleaf vegetation shows little trend in NEE but some variability between 100 year periods. Other vegetation types (not shown) are generally close to zero NEE after the first 100 years.

The slightly positive NEE flux to the atmosphere is balanced by a decrease in the total carbon across all pools (Fig. 6b), which is dominated by carbon loss from the passive soil pool (which has the longest turnover time). The slow soil pool and plant wood pool show much smaller differences over time, being a carbon gain and a carbon loss respectively. There is a suggestion of centennial scale variability in these pools which contributes to the decadal to centennial scale variability seen in the total carbon and likely explains the small gain in total carbon over the last 150 years of the simulation. Around two thirds of the carbon loss in the passive soil pool can be attributed to evergreen broadleaf tiles, consistent with this type contributing the largest non-zero NEE at the end of the simulation.

The behaviour of the nitrogen pools (not shown) is broadly similar to the carbon pools with nitrogen loss from the passive soil pool, again largely from the evergreen broadleaf vegetation type. This loss is offset, to a greater extent than for carbon, by increases in nitrogen in the slow soil pool, primarily for the tundra vegetation type. The trend in pools is a little different for phosphorus with both the passive and slow soil pools growing, while the inorganic phosphorus pools are declining. As for nitrogen the slow soil pool change is dominated by the tundra vegetation type but the other pool changes are split more evenly across a range of vegetation types.

GMDD
8, 8063–8116, 2015

4.2.3 Flux distribution and variability

The zonal mean GPP, plant and soil respiration over the last 500 years for the ProgLAI case is shown in Fig. 7a along with the GPP for the PresLAI case. The GPP distribution is broadly similar for both cases with maximum GPP in the tropics. However ProgLAI gives relatively higher GPP in the mid latitudes (40–60°) and lower GPP in the tropics than PresLAI. Plant respiration generally exceeds soil respiration in the tropics but tends to be smaller than soil respiration at mid-high latitudes.

The difference in GPP can be understood when the prognostic LAI is compared to the LAI values used in the prescribed (PresLAI) case (Fig. 7b). In the prescribed LAI case, the same LAI is used for all tiles within a grid-cell regardless of vegetation type, varying seasonally but not from year to year. Zonally averaged, the prescribed LAI is largest in the tropics, peaking at over 3.0, with annual values closer to 1.0 in the mid latitudes. In ProgLAI, the simulated LAI values are lower in the tropics than those prescribed for all vegetation types. This contrasts with the simulated LAI in the mid-latitudes when all vegetation types show as large or much larger values than those prescribed. In general the evergreen tree types show larger LAI than the other vegetation types; C4 grass is particularly low over much of its geographical range. It appears that C4 grass is more sensitive to low rainfall than co-located C3 grass, especially when CABLE is run with prognostic v_{cmax}. While C4 vegetation is annual and expected to die-back under dry conditions, CABLE does not appear capable of re-growing the vegetation when rainfall does occur. Some improvement in the simulation might be achieved through parameter tuning, but revision of the model formulation for C4 plants may also be required.

Land carbon fluxes are highly seasonal and this is captured by the model; Fig. 8 shows NEE for the final 100 years of the simulation. In the extra-tropics NEE is positive in winter and negative in summer (driven by available radiation), while in the tropics the NEE seasonality follows precipitation, with carbon uptake in the wet season and release in the dry season. With the exception of the southern extratropics, the NEE seasonality is smaller in magnitude for the ProgLAI case than for the PresLAI case. In

GMDD
8, 8063–8116, 2015

the northern extratropics ProgLAI shows a longer growing season but with less uptake in June and July, while positive fluxes in winter are similar to the PresLAI case. In the tropics both carbon uptake and release are smaller for ProgLAI, reflecting the lower simulated LAI in the tropics. In the southern extratropics, the larger NEE seasonality in ProgLAI will not have a large impact on the total carbon flux to the atmosphere since the southern extratropical land area is very small.

Including prognostic LAI in the simulation changes the interannual variability (IAV) of the land carbon fluxes. For global fluxes (Table 2), the standard deviation of annual GPP in the ProgLAI case is 60 % larger than in the PresLAI case. Variability in the respiration fluxes is also larger for ProgLAI, particularly for the leaf respiration. However, for global NEE the ProgLAI case gives slightly smaller standard deviation than PresLAI because GPP and leaf respiration are strongly positively correlated in the ProgLAI case, driven by the interannual variations in LAI. In the PresLAI case, with fixed LAI from year to year, the relatively small interannual variability in leaf respiration appears to be most strongly driven by temperature and has a moderate negative correlation with interannual variations in GPP. Although the IAV of global NEE is smaller for ProgLAI than PresLAI, ProgLAI shows generally larger standard deviation of NEE at mid-high latitudes than PresLAI (Fig. 9a and b). Also shown in Fig. 9c and d is the autocorrelation of NEE for 1 year lag. This shows larger positive correlation for ProgLAI than PresLAI, with the large correlations located mainly in semi-arid regions. Larger correlations for ProgLAI are expected; a year of large GPP and consequently more carbon uptake will lead to increased LAI and a tendency to maintaining large GPP and carbon uptake in the following year. The location of the larger correlations suggests this process is most important for regions where the vegetation is more marginal.

The impact of climate variability on NEE is seen in Fig. 10 which shows the correlation between NEE and precipitation or screen-level temperature for the ProgLAI case. The correlations are similar in pattern for PresLAI and generally slightly stronger than for ProgLAI (suggesting that in ProgLAI the IAV driven by climate is slightly moderated by the autocorrelation in NEE generated by LAI variability). There are strong negative

GMDD
8, 8063–8116, 2015

correlations with precipitation in regions where the rainfall is generally lower and plant growth is water-limited, such as at the margins of deserts. In the northern high latitudes the correlation with precipitation becomes positive. With water limitation unlikely in this region, low precipitation is likely associated with less cloud and more sunshine leading to greater photosynthesis and more negative NEE. The NEE correlation with temperature is positive almost everywhere and largest in the tropics. This is presumably due to the temperature dependence of respiration.

4.3 Ocean carbon

4.3.1 Temporal evolution and the global air–sea carbon flux

WOMBAT conserves the biogeochemical tracers in the ocean, which means the rate of change in the total carbon in the ocean equals the net sea–air flux, noting that the sea–air flux is negative for CO_2 into the ocean, consistent with land fluxes (NEE). The temporal evolution of the global sea–air flux of carbon in the ESM simulations is shown in Fig. 11a. Over the simulation period there is net flux of carbon out of the ocean, which is declining as the ocean slowly equilibrates with the atmosphere. By the end of the simulation, the net outgassing of carbon from the ocean is about 0.6 $\mathrm{Pg\,C\,yr^{-1}}$. As the equilibration time is set by the millennium time-scale of deep water circulation, existing computational resources are insufficient to allow the ESM simulation to reach full carbon equilibrium ($\sim$ 4000 years). We explored using the ocean initial state from an ocean-only simulation driven by climatological atmospheric re-analysis fields. However, our ESM climate was substantially different from the re-analysis fields and this simulation, displaying a large drift in the simulated carbon flux.

Within WOMBAT, if particulate organic matter and calcium carbonate are not remineralized before reaching the seafloor they can accumulate in the sediments. Our simulations show that the carbon in the sediments are stable and small (Fig. 11b) relative to the total amount of carbon dissolved in seawater ($\approx$ 37 000 Pg C; Ciais et al., 2013). Therefore, it is only the net sea–air flux of carbon that alters the total amount of carbon

GMDD
8, 8063–8116, 2015

dissolved in the ocean in our simulations. While there is a slow decline in the global mean sea–air carbon flux, the upper ocean dynamics have largely stabilised as shown by no trend in the simulated annual mean primary productivity (Fig. 11c), with an end of the simulation value of around 51 $\mathrm{Pg\,C\,yr^{-1}}$. This is consistent with global estimates of primary productivity of between 45–50 $\mathrm{Pg\,C\,yr^{-1}}$ (e.g. Carr et al., 2006).

4.3.2 Surface field Assessment

To assess our ocean carbon cycle simulation and CMIP5 simulations (Taylor et al., 2012) against observations, we use a Taylor diagram (Taylor, 2001). This allows us to summarise the bias, relative variability and correlations. Figure 12 shows the Taylor diagram comparing the annual mean surface nitrate, oxygen, alkalinity, DIC, temperature and salinity fields. Overlain on this plot are also the median values from CMIP5 assessed against observations. The radial distance is the spatial standard deviation of the ACCESS-ESM1 simulation or the CMIP5 median, normalized by the standard deviation of observations. The angle from the x axis shows the spatial correlation coefficient between the model (and CMIP5), and the observations. The colours represent the relative difference in the globally averaged values between our simulation (and CMIP5) and observations calculated as (mean_model – mean_reference)/mean_reference; positive values suggest that the model is overestimating the observations and negative values, underestimating. The observations for nitrate, temperature and salinity come from the World Ocean Atlas climatology (WOA2005; Garcia et al., 2006a, b), while pre-industrial DIC and alkalinity are from GLODAP (Key et al., 2004). The individual CMIP5 models used to calculate the multi-model median fields, are: CanESM2, GFDL-ESM2M, HadGEM2-CC, HadGEM2-ES, IPSL-CM5A-LR, IPSL-CM5A-MR, IPSL-CM5B-LR, MPI-ESM-LR, MPI-ESM-MR (Anav et al., 2013). In this paper we only used the first ensemble member of each CMIP5 model. Furthermore, only the surface fields are assessed because by the last century of the ACCESS-ESM1 simulation they show no significant drift.

GMDD
8, 8063–8116, 2015

Encouragingly all variables from the ACCESS-ESM1 simulation show correlations with the observations of close to 0.6 or better. SST shows a very high correlation ($R > 0.98$) with observations, in fact having a better correlation and lower bias than the median of the CMIP5 models, and a very similar magnitude of variability. In contrast, salinity appears to be underestimated in terms of variability and mean value when compared with the observations. However in comparison with the median of the CMIP5 models we see better correlation and smaller biases. These biases are perhaps unsurprising given challenges with capturing well the hydrological cycle in ESMs (Trenberth et al., 2003). The poor representation of salinity in our simulations (and CMIP5) translates to a poor representation of ALK, and accounts for the majority of the bias. While we could reduce the alkalinity bias by altering the export of calcium carbonate from the upper ocean, reducing the salinity bias would be a more effective way of improving alkalinity.

DIC in ACCESS-ESM1 shows a good correlation with observations (Fig. 12), comparable with CMIP5, but overestimates the magnitude of the variability when compared with CMIP5 and observations. The underestimation of the mean value, also seen in CMIP5, may be related to the alkalinity bias enhancing the outgassing of carbon from the upper ocean relative to the observations. In comparison to the observations and CMIP5, nitrate is poorly represented in ACCESS-ESM1 with a large overestimation. This overestimation is much larger than the median from CMIP5 which conversely underestimates the observed mean value. Despite a poor representation of nitrate, this does not translate to significant biases in primary productivity. This suggests that this excess nitrate in the surface ocean is occurring in regions where nutrients are already replete. These larger values in nitrate may be related to the export of particulate organic carbon.

While assessing the simulated values with the median CMIP5 values provides valuable insight, it does not allow us to assess the skill of our model when compared with individual CMIP5 models. To this end the simulated state variables of the carbon system, DIC and ALK are compared with individual CMIP5 models (Fig. 13). For DIC, we

GMDD
8, 8063–8116, 2015

see that our simulation sits in the middle of the CMIP5 correlation values but shows the best estimate of the magnitude of the variability. The DIC biases in the CMIP5 models show a large range, that both under and overestimate the mean value. Our simulation, which underestimates the mean value, is comparable in magnitude to those models that also underestimate the mean value. The simulated ALK (Fig. 13b) shows a similar correlation as the CMIP5 models, but shows a larger variability than most, at the top end of the CMIP5 range. All CMIP5 models underestimate the mean ALK value compared to the observations; our simulation gives a larger underestimation than most models, but is within the range of CMIP5. As discussed earlier this bias is likely related to our bias in surface salinity, and appears to be a common feature of these simulations. Overall, our simulation has comparable skill to the existing CMIP5 models.

4.3.3 Sea-air carbon flux variability

The sea–air carbon flux is shown in Fig. 14 for the last century of the simulation (901–1000). The simulations show outgassing in the tropical ocean and in the Southern Ocean and uptake in the Southern and Northern Hemispheres. This spatial pattern of sea–air fluxes is in very good agreement with the integrated zonal sea–air fluxes estimated by Gruber et al. (2009). The interannual variability (1 sigma) was computed by removing the seasonal monthly climatology, calculated from the last century of the simulation, from the monthly fluxes. The resulting fluxes were then averaged into annual fluxes from which the standard deviation in the variability was determined. Regions of high variability include the tropical Pacific, the North Atlantic and the upwelling regions of Java, Arabia, South America and Africa. There is also a band of elevated variability in the Southern Ocean but it is significantly less than the high variability areas in the tropics.

GMDD
8, 8063–8116, 2015

5 Conclusion and future model development

Documentation of ACCESS-ESM1 and its performance under pre-industrial, prescribed atmospheric CO_2 conditions is important for ongoing work with this model version. In this paper two ACCESS-ESM1 simulations were compared; both used the same ocean biogeochemistry and the land carbon module with nutrient limitation (N and P) active but one used prescribed LAI and the other prognostic LAI. Simulating LAI (ProgLAI) increased interannual variability in GPP and respiration fluxes, but not in global total NEE, and also gave a slight warming of the climate. ProgLAI tended to underestimate the LAI in the tropics and overestimate LAI at high latitudes, compared to the dataset used in the prescribed LAI case. The different LAI distribution impacted the spatial distribution and seasonal cycle of carbon fluxes. Despite the apparent biases in the simulation of leaf area index (in ProgLAI), this is our preferred configuration because it is important that LAI is responsive to climate, especially for scenario simulations out to 2100. Overall, the analysis presented here, and for the historical period (Ziehn et al., 2015) shows that the land carbon module provides realistic simulations of land carbon exchange.

Analysis of the pre-industrial simulation has highlighted some issues with the ACCESS-ESM1 carbon models and how biases in the physical model simulation can contribute to a poor simulation of carbon fluxes. For land carbon, a high priority is to fix the inability of CABLE to conserve carbon in situations where moisture is insufficient to maintain vegetation and to confirm whether land carbon fluxes are too sensitive to climate (particularly rainfall) variability. Development priorities for CABLE in future ACCESS-ESM versions are implementation of land use change, the ability for phenology to respond to climate and improved nutrient forcing (e.g. temporally varying input fluxes).

In the ocean we see reasonable agreement with observations, and results that fall within the range of existing CMIP5 models for DIC and alkalinity. The spatial pattern of pre-industrial sea–air carbon fluxes shows very good agreement with published stud-

GMDD
8, 8063–8116, 2015

ies, while primary productivity is close to the observed value. Nevertheless there are outstanding issues to be addressed in the ocean: (a) reducing salinity biases would improve the simulated values of alkalinity and DIC, bringing these closer to the observations; and (b) reducing the excess of surface nitrate, potentially through modifying the particulate organic carbon export. Furthermore we see a recognised need to add additional complexity, in terms of phytoplankton and zooplankton classes, to capture the potential impacts related to projected changes in the marine environment such as ocean acidification (e.g. Matear and Lenton, 2014).

It is clear from our simulations that our model has yet to fully reach quasi-steady state, despite more than 1000 years of simulation. At present, computational limitations inhibit our ability to optimise the model behaviour and produce carbon fields that are equilibrated with the pre-industrial atmosphere. Therefore in the longer term, we need to develop better ways to tune the carbon models and accelerate the convergence of both the land and ocean carbon models to steady state (e.g. Fang et al., 2015).

At present the next physical model version of ACCESS (ACCESS-CM2) is currently being developed in preparation for CMIP6. The land and ocean carbon cycles presented here will form the basis for ACCESS-ESM2.

Code availability

Code availability varies for different components of ACCESS-ESM1. The UM is licensed by the UK Met Office and is not freely available. CABLE2 is available from https://trac.nci.org.au/svn/cable/. See https://trac.nci.org.au/trac/cable/wiki/CableRegistration for information on registering to use the CABLE repository. MOM4p1 and CICE are freely available under applicable registration or copyright conditions. For MOM4p1 see http://data1.gfdl.noaa.gov/~arl/pubrel/r/mom4p1/src/mom4p1/doc/mom4_manual.html. For CICE see http://oceans11.lanl.gov/trac/CICE. For access to the MOM4p1 code with WOMBAT as used for ACCESS-ESM1, please contact Hailin Yan (Hailin.Yan@csiro.au). The OASIS3-MCT 2.0 coupler code is available from http://oasis.enes.org.

GMDD
8, 8063–8116, 2015

The Supplement related to this article is available online at doi:10.5194/gmdd-8-8063-2015-supplement.

Acknowledgements. This research is supported by the Australian Government Department of the Environment, the Bureau of Meteorology and CSIRO through the Australian Climate Change Science Programme. The research was undertaken on the NCI National Facility in Canberra, Australia, which is supported by the Australian Commonwealth Government. The authors wish to acknowledge use of the Ferret program for some of the analysis and graphics in this paper. Ferret is a product of NOAA's Pacific Marine Environmental Laboratory. (Information is available at http://ferret.pmel.noaa.gov/Ferret/). Ashok Luhar provided helpful feedback on the manuscript. Mark Collier implemented the PCDMI metrics package, which was used for the comparison of atmospheric variables between ACCESS model versions. Arnold Sullivan helped produce some of the figures.

References

Anav, A., Friedlingstein, P., Kidston, M., Bopp, L., Ciais, P., Cox, P., Jones, C., Jung, M., Myneni, R., and Zhu, Z.: Evaluating the land and ocean components of the global carbon cycle in the CMIP5 Earth System Models, J. Climate, 26, 6801–6843, 2013. 8065, 8088

Anderson, L. A. and Sarmiento, J. L.: Redfield ratios of remineralization determined by nutrient data analysis, Global Biogeochem. Cy., 8, 65–80, 1994. 8073

Arora, V. K., Boer, G. J., Friedlingstein, P., Eby, M., Jones, C. D., Christian, J. R., Bonan, G., Bopp, L., Brovkin, V., Cadule, P., Hajima, T., Ilyina, T., Lindsay, K., Tjiputra, J. F., and Wu, T.: Carbon-concentration and carbon-climate feedbacks in CMIP5 Earth System Models, J. Climate, 26, 5289–5314, 2013. 8065

Bi, D., Marsland, S. J., Uotila, P., O'Farrell, S., Fiedler, R., Sullivan, A., Griffies, S. M., Zhou, X., and Hirst, A. C.: ACCESS-OM: the ocean and sea-ice core of the ACCESS coupled model, Aust. Meteor. Oceanogr. J., 63, 213–232, 2013a. 8067, 8069, 8075

Bi, D., Dix, M., Marsland, S. J., O'Farrell, S., Rashid, H. A., Uotila, P., Hirst, A. C., Kowalczyk, E., Golebiewski, M., Sullivan, A., Yan, H., Hannah, N., Franklin, C., Sun, Z., Vohralik, P., Watterson, I., Zhou, X., Fiedler, R., Collier, M., Ma, Y., Noonan, J., Stevens, L., Uhe, P., Zhu, H.,

GMDD
8, 8063–8116, 2015

Griffies, S. M., Hill, R., Harris, C., and Puri, K.: The ACCESS coupled model: description, control climate and evaluation, Aust. Meteor. Oceanogr. J., 63, 41–64, 2013b. 8065, 8067, 8081

Boer, G. J. and Arora, V. K.: Feedbacks in emission-driven and concentration-driven global carbon budgets, J. Climate, 26, 3326–3314, doi:10.1175/JCLI-D-12-00365.1, 2012. 8065

Boyer, T. P., Antonov, J. I., Baranova, O. K., Garcia, H. E., Johnson, D. R., Locarnini, R. A., Mishonov, A. V., O'Brien, T., Seidov, D., and Smolyar, I. V.: World Ocean Database 2009, Vol. 66, NOAA Atlas NESDIS, US Gov. Printing Office, Wash., D.C., available at: http://www.vliz.be/imis/imis.php?module=ref&refid=205411 (last access: 16 September 2015), 2009. 8081

Carr, M.-E., Friedrichs, M. A. M., Schmeltz, M., Aita, M. N., Antoine, D., Arrigo, K. R., Asanuma, I., Aumont, O., Barber, R., Behrenfeld, M., Bidigare, R., Buitenhuis, E., Campbell, J., Ciotti, A., Dierssen, H., Dowell, M., Dunne, J., Esaias, W., Gentili, B., Gregg, W., Groom, S., Hoepffner, N., Ishizaka, J., Kameda, T., Le Quéré, C., Lohrenz, S., Marra, J., Mélin, F., Moore, J., Morel, A., Reddy, T. E., Ryan, J., Scardi, M., Smyth, T., Turpie, K., Tilstone, G., Waters, K., and Yamanaka, Y.: A comparison of global estimates of marine primary production from ocean color, Deep-Sea Res. Pt. II, 53, 741–770, 2006. 8088

Ciais, P., Sabine, C., Bala, G., Bopp, L., Brovkin, V., Canadell, J., Chhabra, A., DeFries, R., Galloway, J., Heimann, M., Jobes, C., Le Quéré, C., Myneni, R. B., Piao, S., and Thornton, P.: Carbon and other biogeochemical cycles, in: Climate Change 2013: The Physical Science Basis. Contribution of Working Group I to the Fifth Assessment Report of the Intergovernmental Panel on Climate Change, edited by: Stocker, T. F., Qin, D., Plattner, G.-K., Tignor, M., Allen, S. K., Boschung, J., Nauels, A., Xia, Y., Bex, V., and Midgley, P. M., Cambridge University Press, Cambridge, UK and New York, NY, USA, 465–570, 2013. 8087

Cox, P. D., Betts, R. A., Jones, C. D., Spall, S. A., and Totterdell, I. J.: Acceleration of global warming due to carbon-cycle feedbacks in a coupled climate model, Nature, 408, 184–187, 2000. 8065

Dix, M., Vohralik, P., Bi, D., Rashid, H., Marsland, S., O'Farrell, S., Uotila, P., Hirst, T., Kowalczyk, E., Sullivan, A., Yan, H., Franklin, C., Sun, Z., Watterson, I., Collier, M., Noonan, J., Rotstayn, L., Stevens, L., Uhe, P., and Puri, K.: The ACCESS coupled model: documentation of core CMIP5 simulations and initial results, Aust. Meteor. Oceanogr. J., 63, 83–99, 2013. 8065, 8067

GMDD
8, 8063–8116, 2015

Exbrayat, J.-F., Pitman, A. J., Abramowitz, G., and Wang, Y.-P.: Sensitivity of net ecosystem exchange and heterotrophic respiration to parameterization uncertainty, J. Geophys. Res.-Atmos., 118, 1–12, doi:10.1029/2012JD018122, 2013. 8072

Fang, Y., Liu, C., and Leung, L. R.: Accelerating the spin-up of the coupled carbon and nitrogen cycle model in CLM4, Geosci. Model Dev., 8, 781–789, doi:10.5194/gmd-8-781-2015, 2015. 8092

Flato, G., Marotzke, J., Abiodun, B., Braconnot, P., Chou, S., Collins, W., Cox, P., Driouech, F., Emori, S., Eyring, V., Forest, C., Gleckler, P., Guilyardi, E., Jakob, C., Kattsov, V., Reason, C., and Rummukainen, M.: Evaluation of Climate Models, in: Climate Change 2013: The Physical Science Basis. Contribution of Working Group I to the Fifth Assessment Report of the Intergovernmental Panel on Climate Change, edited by: Stocker, T. F., Qin, D., Plattner, G.-K., Tignor, M., Allen, S., Boschung, J., Nauels, A., Xia, Y., Bex, V., and Midgley, P., 741–866, Cambridge University Press, Cambridge, UK and New York, NY, USA, 2013. 8079

Friedlingstein, P., Bopp, L., Ciais, P., Dufresne, J.-L., Fairhead, L., LeTreut, H., Monfray, P., and Orr, J.: Positive feedback between future climate change and the carbon cycle, Geophys. Res. Lett., 28, 1543–1546, 2001. 8065

Friedlingstein, P., Cox, P., Betts, R., Bopp, L., von Bloch, W., Brovkin, V., Cadule, P., Doney, S., Eby, M., Fung, I., Bala, G., John, J., Jones, C., Joos, F., Kato, T., Kawamiya, M., Knorr, W., Lindsay, K., Matthews, H. D., Raddatz, T., Rayner, P., Reick, C., Roeckner, E., Schnitzler, K.-G., Schnur, R., Strassmann, K., Weaver, A. J., Yoshikawa, C., and Zeng, N.: Climate–carbon cycle feedback analysis: results from the C^4MIP model intercomparison, J. Climate, 19, 3337–3353, doi:10.1175/JCLI3800.1, 2006. 8065

Friedlingstein, P., Meinshausen, M., Arora, V. K., Jones, C. D., Anav, A., Liddicoat, S. K., and Knuitti, R.: Uncertainties in CMIP5 climate projections due to carbon cycle feedbacks, J. Climate, 27, 511–526, 2014. 8065

Garcia, H., Locarnini, R., and Boyer, T.: World ocean atlas 2005, Volume 3: Dissolved oxygen, apparent oxygen utilization, in: NOAA Atlas NESDIS 63, edited by: Levitus, S., US Government Printing Office, Washington, D.C., 342 pp., 2006a. 8077, 8088

Garcia, H., Locarnini, R., Boyer, T., and Antonov, J.: World ocean atlas 2005, Volume 4: Nutrients (phosphate, nitrate, silicate), in: NOAA Atlas NESDIS 63, edited by: Levitus, S., US Government Printing Office, Washington, D.C., 396 pp., 2006b. 8077, 8088

Gleckler, P. J., Taylor, K. E., and Doutriaux, C.: Performance metrics for climate models, J. Geophys. Res., 113, D06104, doi:10.1029/2007JD008972, 2008. 8079

GMDD
8, 8063–8116, 2015

Griffies, S. M.: Elements of MOM4p1, GFDL Ocean Group, Tech. Rep. No. 6, NOAA/Geophysical Fluid Dynamics Laboratory, Princeton, USA, 2009. 8067

Gruber, N., Gloor, M., Fletcher, S. E. M., Doney, S. C., Dutkiewicz, S., Follows, M. J., Gerber, M., Jacobson, A. R., Joos, F., Lindsay, K., Menemenlis, D., Mouchet, A., Muller, S. A., Sarmiento, J. L., and Takahashi, T.: Oceanic sources, sinks, and transport of atmospheric CO_2, Global Biogeochem. Cy., 23, GB1005, doi:10.1029/2008gb003349, 2009. 8090

Hewitt, H. T., Copsey, D., Culverwell, I. D., Harris, C. M., Hill, R. S. R., Keen, A. B., McLaren, A. J., and Hunke, E. C.: Design and implementation of the infrastructure of HadGEM3: the next-generation Met Office climate modelling system, Geosci. Model Dev., 4, 223–253, doi:10.5194/gmd-4-223-2011, 2011. 8067

Huang, M., Piao, S., Sun, Y., Ciais, P., Cheng, L., Mao, J., Poulter, B., Shi, X., Zeng, Z., and Wang, Y.: Change in terrestrial ecosystem water-use efficiency over the last three decades, Glob. Change Biol., 21, 2366–2378, doi:10.1111/gcb.12873, 2015. 8073

Huneeus, N., Schulz, M., Balkanski, Y., Griesfeller, J., Prospero, J., Kinne, S., Bauer, S., Boucher, O., Chin, M., Dentener, F., Diehl, T., Easter, R., Fillmore, D., Ghan, S., Ginoux, P., Grini, A., Horowitz, L., Koch, D., Krol, M. C., Landing, W., Liu, X., Mahowald, N., Miller, R., Morcrette, J.-J., Myhre, G., Penner, J., Perlwitz, J., Stier, P., Takemura, T., and Zender, C. S.: Global dust model intercomparison in AeroCom phase I, Atmos. Chem. Phys., 11, 7781–7816, doi:10.5194/acp-11-7781-2011, 2011. 8068

Hunke, E. C. and Lipscomb, W. H.: CICE: The Los Alamos sea ice model documentation and software user's manual, Version 4.1, LA-CC-06-012, Los Alamos National Laboratory, N.M., 2010. 8067

Jones, C., Robertson, E., Arora, V., Friedlingstein, P., Shevliakova, E., Bopp, L., Brovkin, V., Hajima, T., Kato, E., Kawamiya, M., Liddicoat, S., Lindsay, K., Reick, C. H., Roelandt, C., Segschneider, J., and Tjiputra, J.: Twenty-first-century compatible CO_2 emissions and airborne fraction simulated by CMIP5 Earth System Models under four representative concentration pathways, J. Climate, 26, 4398–4413, 2013. 8065

Jones, C. D., Hughes, J. K., Bellouin, N., Hardiman, S. C., Jones, G. S., Knight, J., Liddicoat, S., O'Connor, F. M., Andres, R. J., Bell, C., Boo, K.-O., Bozzo, A., Butchart, N., Cadule, P., Corbin, K. D., Doutriaux-Boucher, M., Friedlingstein, P., Gornall, J., Gray, L., Halloran, P. R., Hurtt, G., Ingram, W. J., Lamarque, J.-F., Law, R. M., Meinshausen, M., Osprey, S., Palin, E. J., Parsons Chini, L., Raddatz, T., Sanderson, M. G., Sellar, A. A., Schurer, A., Valdes, P., Wood, N., Woodward, S., Yoshioka, M., and Zerroukat, M.: The

GMDD
8, 8063–8116, 2015

HadGEM2-ES implementation of CMIP5 centennial simulations, Geosci. Model Dev., 4, 543–570, doi:10.5194/gmd-4-543-2011, 2011. 8075

Kattge, J., Knorr, W., Raddatz, T., and Wirth, C.: Quantifying photosynthetic capacity and its relationship to leaf nitrogen content for global-scale terrestrial biosphere models, Glob. Change Biol., 15, 976–991, doi:10.1111/j.1365-2486.2008.01744.x, 2009. 8072

Kelly, R. H., Parton, W. J., Hartman, M. D., Stretch, L. K., Ojima, D. S., and Schimel, D. S.: Intra-annual and interannual variability of ecosystem processes in shortgrass steppe, J. Geophys. Res., 105, 20093–20100, doi:10.1029/2000JD900259, 2000. 8072

Key, R. M., Kozyr, A., Sabine, C. L., Lee, K., Wanninkhof, R., Bullister, J. L., Feely, R. A., Millero, F. J., Mordy, C., and Peng, T. H.: A global ocean carbon climatology: results from Global Data Analysis Project (GLODAP), Global Biogeochem. Cy., 18, GB4031, doi:10.1029/2004GB002247, 2004. 8078, 8088

Kowalczyk, E. A., Wang, Y. P., Law, R. M., Davies, H. L., McGregor, J. L., and Abramowitz, G.: The CSIRO Atmosphere Biosphere Land Exchange (CABLE) model for use in climate models and as an offline model, CSIRO Marine and Atmospheric Research technical paper 13, Aspendale, Victoria, Australia, 2006. 8066, 8069

Kowalczyk, E. A., Stevens, L., Law, R. M., Dix, M., Wang, Y. P., Harman, I. N., Haynes, K., Srbinovsky, J., Pak, B., and Ziehn, T.: The land surface model component of ACCESS: description and impact on the simulated surface climatology, Aust. Meteor. Oceanogr. J., 63, 65–82, 2013. 8069, 8070, 8076, 8077, 8081

Lawrence, P. J., Feddema, J. J., Bonan, G. B., Meehl, G. A., O'Neill, B. C., Oleson, K. W., Levis, S., Lawrence, D. M., Kluzek, E., Lindsay, K., and Thornton, P. E.: Simulating the biogeochemical and biogeophysical impacts of transient land cover change and wood harvest in the Community Climate System Model (CCSM4) from 1850 to 2100, J. Climate, 25, 3071–3095, doi:10.1175/JCLI-D-11-00256.1, 2012. 8076

Lenton, A. and Matear, R. J.: Role of the Southern Annular Mode (SAM) in Southern Ocean CO_2 uptake, Global Biogeochem. Cy., 21, GB2016, doi:10.1029/2006GB002714, 2007. 8073

Marsland, S. J., Bi, D., Uotila, P., Fiedler, R., Griffies, S. M., Lorbacher, K., O'Farrell, S., Sullivan, A., Uhe, P., Zhou, X., and Hirst, A. C.: Evaluation of ACCESS climate model ocean diagnostics in CMIP5 simulations, Aust. Meteor. Oceanogr. J., 63, 101–119, 2013. 8067, 8081

GMDD
8, 8063–8116, 2015

Martin, G. M., Milton, S. F., Senior, C. A., Brooks, M. E., Ineson, S., Reichler, T., and Kim, J.: Analysis and reduction of systematic errors through a Seamless approach to modelling weather and climate, J. Climate, 23, 5933–5957, doi:10.1175/2010JCLI3541.1, 2010. 8067

Matear, R. J. and Lenton, A.: Quantifying the impact of ocean acidification on our future climate, Biogeosciences, 11, 3965–3983, doi:10.5194/bg-11-3965-2014, 2014. 8092

O'Kane, T. J., Matear, R. J., Chamberlain, M. A., and Risbey, J. S.: Decadal variability in an OGCM Southern Ocean: intrinsic modes, forced modes and metastable states, Ocean Model., 16, 1–21, doi:10.1016/j.ocemod.2013.04.009, 2013. 8067

Oke, P. R., Griffin, D. A., Schiller, A., Matear, R. J., Fiedler, R., Mansbridge, J., Lenton, A., Cahill, M., Chamberlain, M. A., and Ridgway, K.: Evaluation of a near-global eddy-resolving ocean model, Geosci. Model Dev., 6, 591–615, doi:10.5194/gmd-6-591-2013, 2013. 8066, 8073

Oschlies, A. and Schartau, M.: Basin-scale performance of a locally optimized marine ecosystem model, J. Marine Res., 63, 335–358, 2005. 8101

Puri, K., Dietachmayer, G., Steinle, P., Dix, M., Rikus, L., Logan, L., Naughton, M., Tingwell, C., Xiao, Y., Barras, V., Bermous, I., Bowen, R., Deschamps, L., Franklin, C., Fraser, J., Glowacki, T., Harris, B., Lee, J., Le, T., Roff, G., Sulaiman, A., Sims, H., Sun, X., Sun, Z., Zhu, H., Chattopadhyay, M., and Engel, C.: Implementation of the initial ACCESS numerical weather prediction system, Aust. Meteor. Oceanogr. J., 63, 265–284, 2013. 8065

Shao, P., Zeng, X., Sakaguchi, K., Monson, R. K., and Zeng, X.: Terrestrial carbon cycle: climate relations in eight CMIP5 Earth System Models, J. Climate, 26, 8744–8764, 2013. 8065

Taylor, K. E.: Summarizing multiple aspects of model performance in a single diagram, J. Geophys. Res., 106, 7183–7192, 2001. 8088

Taylor, K. E., Stouffer, R. J., and Meehl, G. A.: An overview of CMIP5 and the experiment design, B. Am. Meteorol. Soc., 93, 485–498, doi:10.1175/BAMS-D-11-00094.1, 2012. 8065, 8088

The HadGEM2 Development Team: G. M. Martin, Bellouin, N., Collins, W. J., Culverwell, I. D., Halloran, P. R., Hardiman, S. C., Hinton, T. J., Jones, C. D., McDonald, R. E., McLaren, A. J., O'Connor, F. M., Roberts, M. J., Rodriguez, J. M., Woodward, S., Best, M. J., Brooks, M. E., Brown, A. R., Butchart, N., Dearden, C., Derbyshire, S. H., Dharssi, I., Doutriaux-Boucher, M., Edwards, J. M., Falloon, P. D., Gedney, N., Gray, L. J., Hewitt, H. T., Hobson, M., Huddleston, M. R., Hughes, J., Ineson, S., Ingram, W. J., James, P. M., Johns, T. C., Johnson, C. E., Jones, A., Jones, C. P., Joshi, M. M., Keen, A. B., Liddicoat, S.,

GMDD
8, 8063–8116, 2015

Lock, A. P., Maidens, A. V., Manners, J. C., Milton, S. F., Rae, J. G. L., Ridley, J. K., Sellar, A., Senior, C. A., Totterdell, I. J., Verhoef, A., Vidale, P. L., and Wiltshire, A.: The HadGEM2 family of Met Office Unified Model climate configurations, Geosci. Model Dev., 4, 723–757, doi:10.5194/gmd-4-723-2011, 2011. 8067

Trenberth, K. E., Dai, A., Rasmussen, R. M., and Parsons, D. B.: The changing character of precipitation, B. Am. Meteorol. Soc., 84, 1205–1217, 2003. 8089

Uotila, P., O'Farrell, S., Marsland, S. J., and Bi, D.: The sea-ice performance of the Australian climate models participating in the CMIP5, Aust. Meteor. Oceanogr. J., 63, 121–143, 2013. 8067, 8081

Valcke, S.: OASIS3 User Guide (prism 2–5), PRISM Support Initiative Report No 3, CERFACS, Toulouse, France, 2006. 8069

Valcke, S.: The OASIS3 coupler: a European climate modelling community software, Geosci. Model Dev., 6, 373–388, doi:10.5194/gmd-6-373-2013, 2013. 8067

Valcke, S., Craig, T., and Coquart, L.: OASIS3-MCT User Guide, OASIS3-MCT_2.0, CERFACS Technical Report TR-CMGC-13-17, CERFACS/CNRS SUC URA No 1875, Toulouse, France, available at: http://pantar.cerfacs.fr/globc/publication/technicalreport/2013/oasis3mct_UserGuide.pdf (last access: 16 September 2015), 2013. 8069

Wang, Y. P. and Leuning, R.: A two-leaf model for canopy conductance, photosynthesis and partitioning of available energy I. Model description and comparison with a multi-layered model, Agr. Forest Meteorol., 91, 89–111, 1998. 8071

Wang, Y. P., Law, R. M., and Pak, B.: A global model of carbon, nitrogen and phosphorus cycles for the terrestrial biosphere, Biogeosciences, 7, 2261–2282, doi:10.5194/bg-7-2261-2010, 2010. 8070, 8072, 8077

Wang, Y. P., Kowalczyk, E., Leuning, R., Abramowitz, G., Raupach, M. R., Pak, B., van Gorsel, E., and Luhar, A.: Diagnosing errors in a land surface model (CABLE) in the time and frequency domains, J. Geophys. Res., 116, G01034, doi:10.1029/2010JG001385, 2011. 8069

Wang, Y. P., Lu, X. J., Wright, I. J., Dai, Y. J., Rayner, P. J., and Reich, P. B.: Correlations among leaf traits provide a significant constraint on the estimate of global gross primary production, Geophys. Res. Lett., 39, L19405, doi:10.1029/2012GL053461, 2012. 8071

Wang, Y. P., Zhang, Q., Pitman, A. J., and Dai, Y. J.: Nitrogen and phosphorus limitation reduces the effects of land use change on land carbon uptake and emission, Environ. Res. Lett., 10, 014001, doi:10.1088/1748-9326/10/014001, 2015. 8073

GMDD
8, 8063–8116, 2015

Wanninkhof, R.: Relationship between wind speed and gas exchange over the ocean, J. Geophys. Res., 97, 7373–7382, doi:10.1029/92JC00188, 1992. 8074
Wilson, D. R., Bushell, A. C., Kerr-Munslow, A. M., Price, J. D., and Morcrette, C. J.: PC2: a prognostic cloud fraction and condensation scheme, I: Scheme description, Q. J. Roy. Meteor. Soc., 134, 2093–2107, 2008. 8067
Woodward, S.: Modeling the atmospheric life cycle and radiative impact of mineral dust in the Hadley Centre climate model, J. Geophys. Res., 106, 18155–18166, doi:10.1029/2000JD900795, 2001. 8068
Woodward, S.: Mineral dust in HadGEM2, Hadley Centre Technical Note 87, Met Office Hadley Centre, Exeter, UK, available at: http://www.metoffice.gov.uk/media/pdf/l/p/HCTN_87.pdf (last access: 12 August 2015), 2011. 8068
Zhang, Q., Wang, Y. P., Pitman, A. J., and Dai, Y. J.: Limitations of nitrogen and phosphorous on the terrestrial carbon uptake in the 20th century, Geophys. Res. Lett., 38, L22701, doi:10.1029/2011GL049244, 2011. 8073
Zhang, Q., Pitman, A. J., Wang, Y. P., Dai, Y. J., and Lawrence, P. J.: The impact of nitrogen and phosphorous limitation on the estimated terrestrial carbon balance and warming of land use change over the last 156 yr, Earth Syst. Dynam., 4, 333–345, doi:10.5194/esd-4-333-2013, 2013. 8071, 8072, 8073, 8075
Zhang, Q., Wang, Y. P., Matear, R. J., Pitman, A. J., and Dai, Y. J.: Nitrogen and phosphorous limitations significantly reduce future allowable CO_2 emissions, Geophys. Res. Lett., 41, 632–637, doi:10.1002/2013GL058352, 2014. 8073, 8075
Zhang, X. Y., Friedl, M. A., Schaaf, C. B., and Strahler, A. H.: Climate controls on vegetation phenological patterns in northern mid- and high latitudes inferred from MODIS data, Glob. Change Biol., 10, 1133–1145, 2004. 8072
Zhang, X. Y., Friedl, M. A., Schaaf, C. B., Strahler, A. H., and Liu, Z.: Monitoring the response of vegetation phenology to precipitation in Africa by coupling MODIS and TRMM instruments, J. Geophys. Res., 110, D12103, doi:10.1029/2004JD005263, 2005. 8072
Ziehn, T., Lenton, A., Law, R. M., Matear, R. M., and Chamberlain, M.: The carbon cycle in the Australian Community Climate and Earth System Simulator (ACCESS-ESM1) – Part 2: Historical simulation, Geosci. Model Dev. Discuss, in preparation, 2015. 8066, 8079, 8091

GMDD
8, 8063–8116, 2015

Table 1. Model Parameters of the BGC model were set to the values optimised in the 1-D model of the Southern Ocean (Oschlies and Schartau, 2005).

Parameter	Units	Value
Phytoplankton model parameters		
Initial slope of P-I curve	$day^{-1}\,(W\,m^{-2})^{-1}$	0.256
Photosynthetically active radiation	–	0.43
Maximum growth rate parameters	day^{-1}, –, C^{-1}	0.27, 1.066, 1.0
Half saturation constant for N uptake	$mmol\,N\,m^{-3}$	0.7
Half saturation constant for Fe uptake	$\mu mol\,Fe\,m^{-3}$	0.1
Phytoplankton mortality	day^{-1}	$0.04\ b^{cT}$
Quadratic mortality	$(mmol\,N\,m^{-3})^{-1}\ day^{-1}$	0.25
Zooplankton model parameters		
Assimilation efficiency	–	0.925
Maximum grazing rate	day^{-1}	1.575
Prey capture rate	$(mmol\,N\,m^{-2})^{-1}\ day^{-1}$	1.6
Quadratic mortality	$(mmol\,N\,m^{-3})^{-1}\ day^{-1}$	0.34
Excretion	day^{-1}	$0.01\ b^{cT}$
Detritus model parameters		
Remineralisation rate (< 180 m)	day^{-1}	$0.048\ b^{cT}$
Remineralisation rate (≥ 180 m)	day^{-1}	$0.024\ b^{cT}$
Sinking velocity	$m\,day^{-1}$	18.0
$CaCO_3$ model parameters		
Remineralisation rate	day^{-1}	0.0035
Sinking velocity	$m\,day^{-1}$	10.0
Inorganic fraction	–	0.08
Fe model parameters		
Scavenging rate	day^{-1}	0.00274
Background	$\mu mol\,Fe\,m^{-3}$	0.1

GMDD
8, 8063–8116, 2015

Table 2. Standard deviation of annual global carbon flux for years 901–1000 in $PgC\,yr^{-1}$.

	PresLAI	ProgLAI
GPP	1.17	1.87
Leaf resp	0.26	0.75
Plant resp	0.17	0.27
Soil resp	0.27	0.32
NEE	1.40	1.21

GMDD
8, 8063–8116, 2015

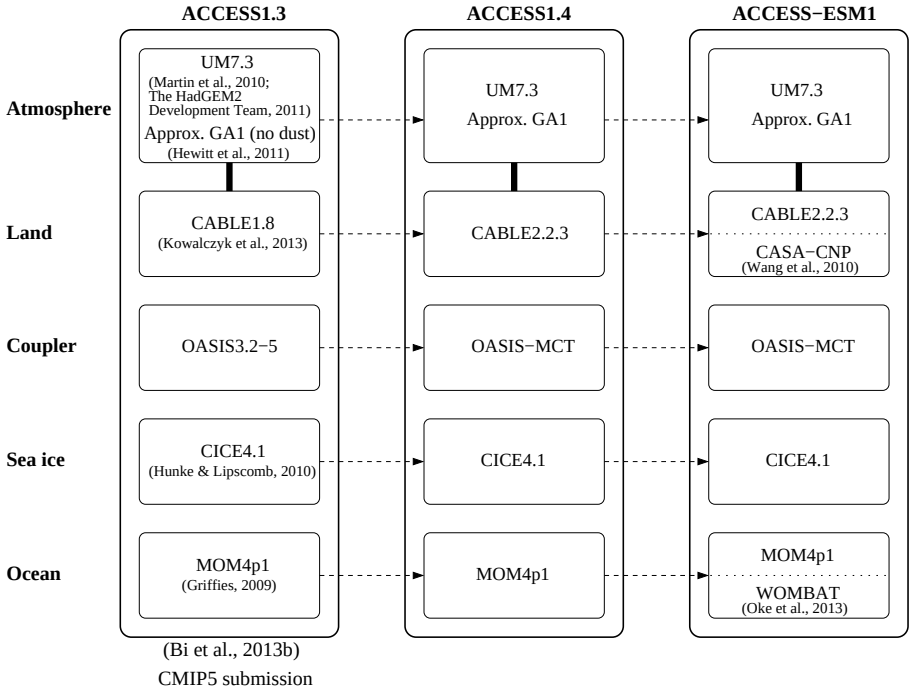

Figure 1. Schematic showing the different component models of ACCESS-ESM1 and the ACCESS versions on which it is dependent.

GMDD
8, 8063–8116, 2015

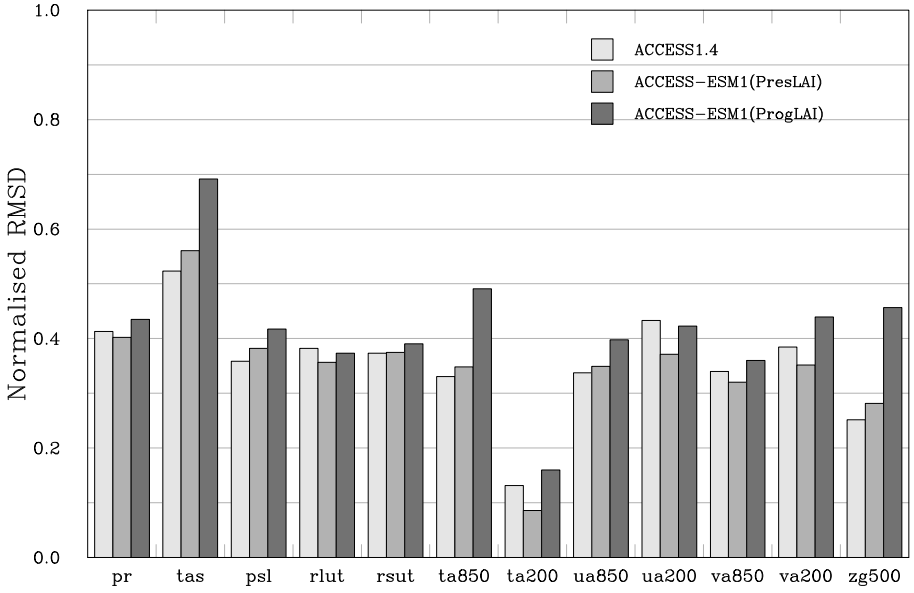

Figure 2. Root mean square difference (RMSD) between atmospheric variables simulated by the model versions listed in the key and those from the ACCESS1.3 pre-industrial simulation normalised by the RMSD between ACCESS1.0 and ACCESS1.3. The variables are precipitation (pr), surface air temperature (tas), sea level pressure (psl), top of atmosphere long-wave radiation (rlut), top of atmosphere reflected short-wave radiation (rsut), air temperature (ta), zonal (ua) and meridional wind (va) at 850 and 200 hPa and geopotential height (zg) at 500 hPa.

GMDD
8, 8063–8116, 2015

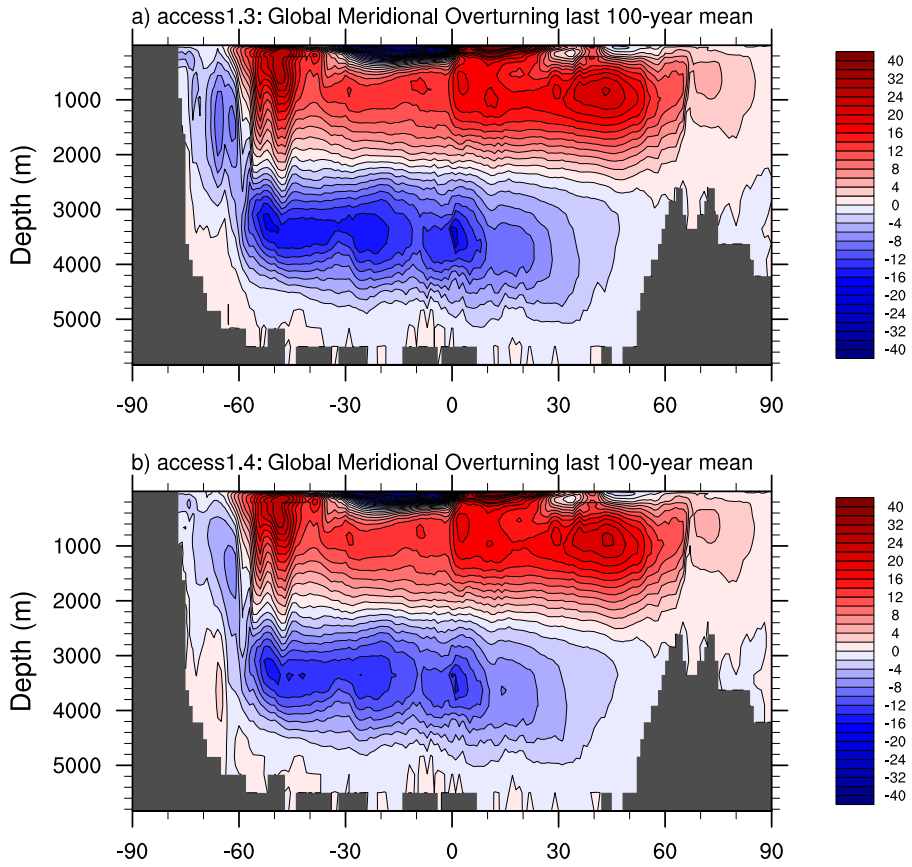

Figure 3. Global Meridional Overturning Streamfunction (Sv) from 100 year average for **(a)** ACCESS1.3 and **(b)** ACCESS1.4 pre-industrial simulations.

GMDD
8, 8063–8116, 2015

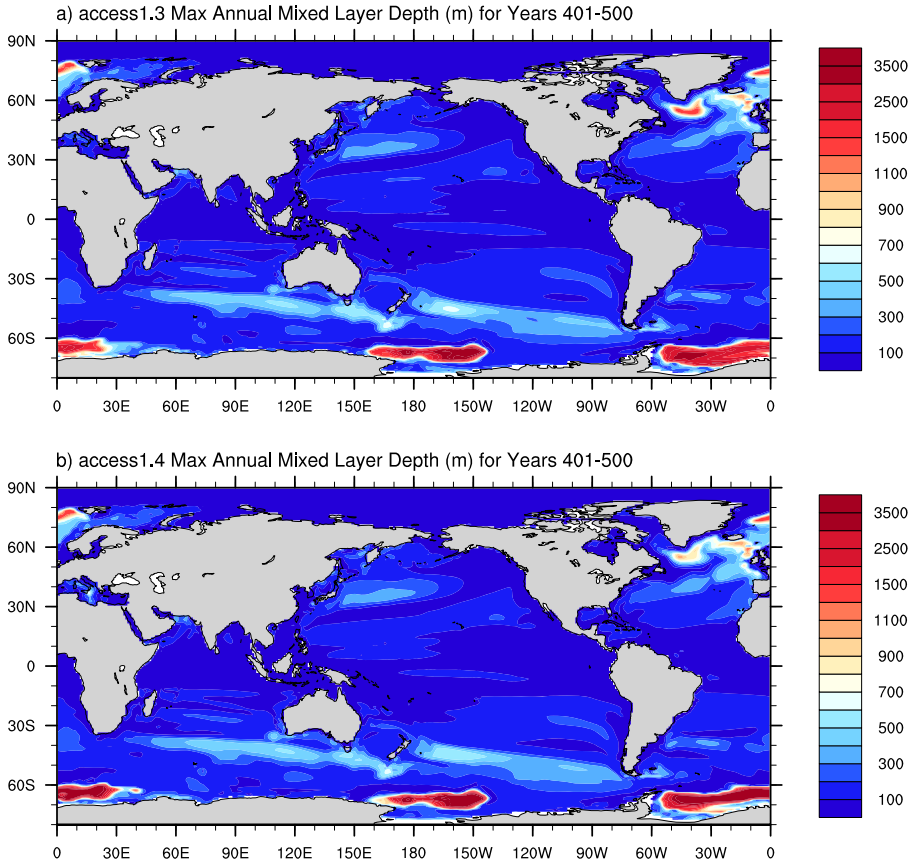

Figure 4. Maximum mixed layer (m) from 100 year average for **(a)** ACCESS1.3 and **(b)** ACCESS1.4 pre-industrial simulations.

GMDD
8, 8063–8116, 2015

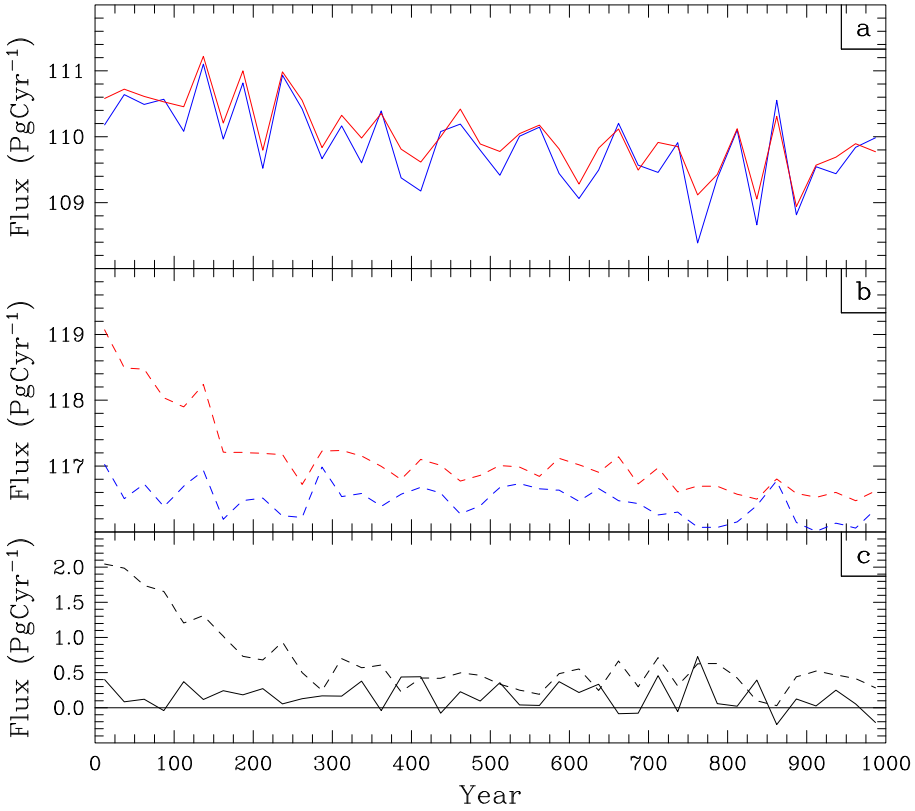

Figure 5. 25 year mean global GPP (blue) and summed respiration (red) in PgC yr^{-1} for the ProgLAI simulation **(a)** and the PresLAI simulation **(b)**. Panel **(c)** shows 25 year mean global NEE in PgC yr^{-1} for ProgLAI (solid) and PresLAI (dashed).

GMDD
8, 8063–8116, 2015

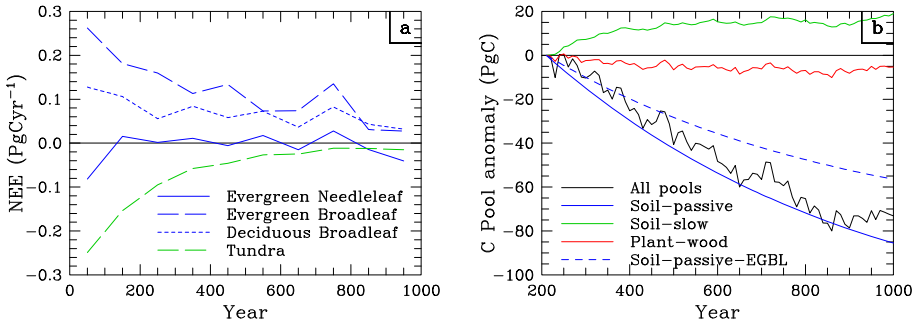

Figure 6. 100 year mean global NEE **(a)** in PgC yr^{-1} for selected vegetation types as listed in the key and carbon pool size **(b)** in PgC at the end of each 10 years relative to year 210 for the sum of all carbon pools (black), and selected carbon pools (passive soil, blue solid; slow soil, green; plant wood, red and passive soil for evergreen broadleaf trees, blue dash) for the ProgLAI simulation. The horizontal black line indicates zero NEE **(a)** and zero C pool anomaly **(b)**.

GMDD
8, 8063–8116, 2015

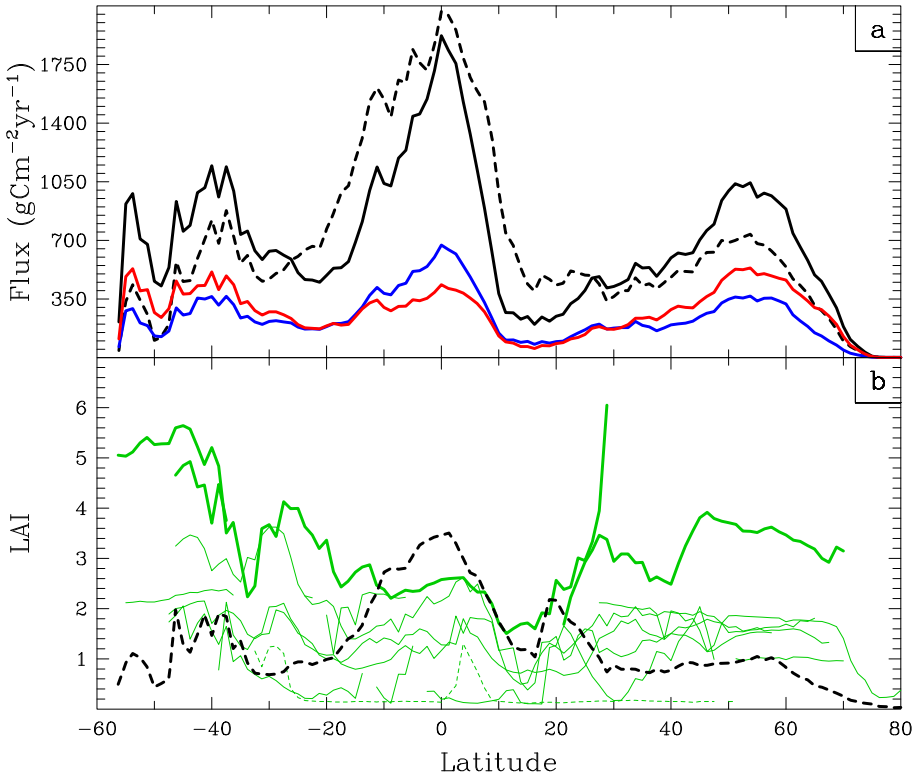

Figure 7. Zonal mean year 501–1000 carbon flux **(a)** in g C m^{-2}yr^{-1} and leaf area index **(b)**. Carbon fluxes are zonally averaged over all land grid-cells, showing from ProgLAI, GPP (black solid), plant respiration (blue) and soil respiration (red) and from PresLAI, GPP (black, dashed). For ProgLAI the LAI is zonally averaged over all tiles for each vegetation type separately (evergreen trees, bold green; C4 grass, dotted green; all other types, solid green). For PresLAI, the LAI is zonally averaged over all land grid-cells (black, dash).

GMDD
8, 8063–8116, 2015

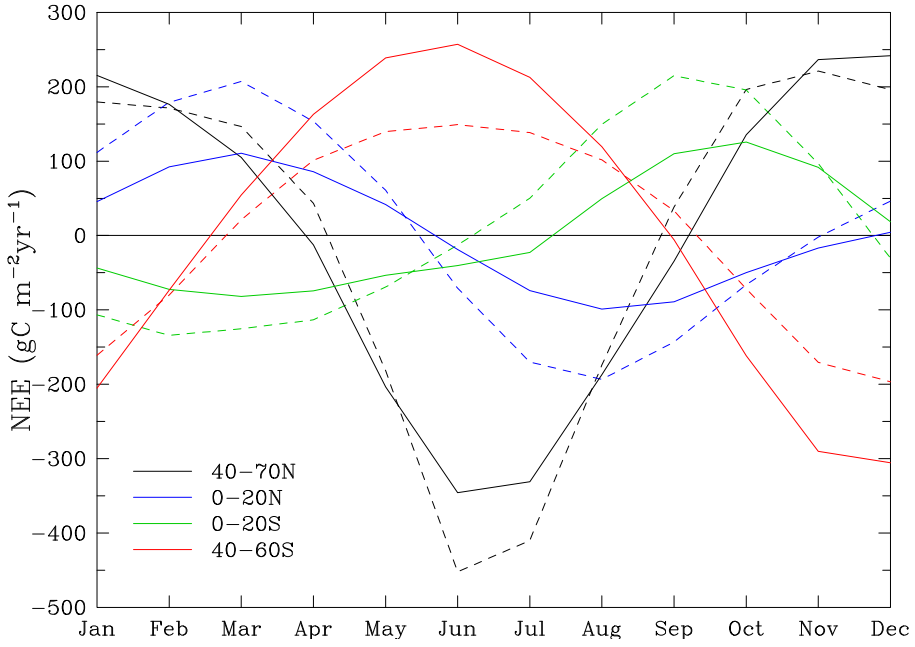

Figure 8. Monthly mean NEE in g C m^{-2}yr^{-1} for years 901–1000 averaged over the land grid-cells in four latitude bands (as listed in the key), for PresLAI (dashed) and ProgLAI (solid).

GMDD
8, 8063–8116, 2015

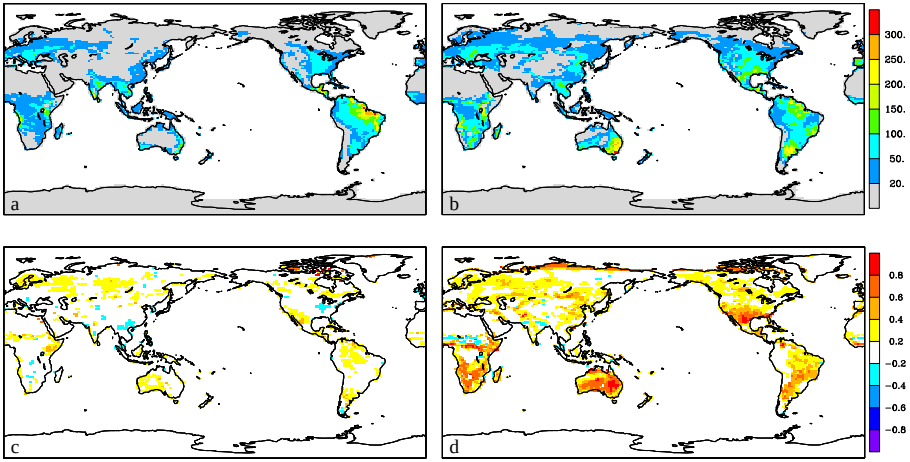

Figure 9. Standard deviation of annual NEE **(a, b)** in $\mathrm{g\,C\,m^{-2}yr^{-1}}$ for years 901–1000 and the autocorrelation for NEE with one year lag **(c, d)** for PresLAI (left) and ProgLAI (right).

GMDD
8, 8063–8116, 2015

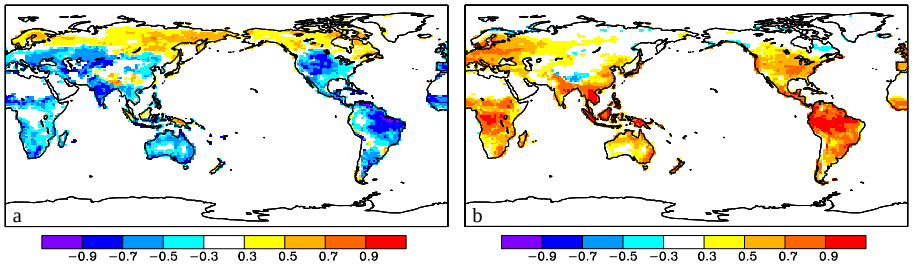

Figure 10. Correlation between annual NEE and **(a)** annual mean precipitation and **(b)** annual mean screen-level temperature for years 901–1000 from the ProgLAI simulation.

GMDD
8, 8063–8116, 2015

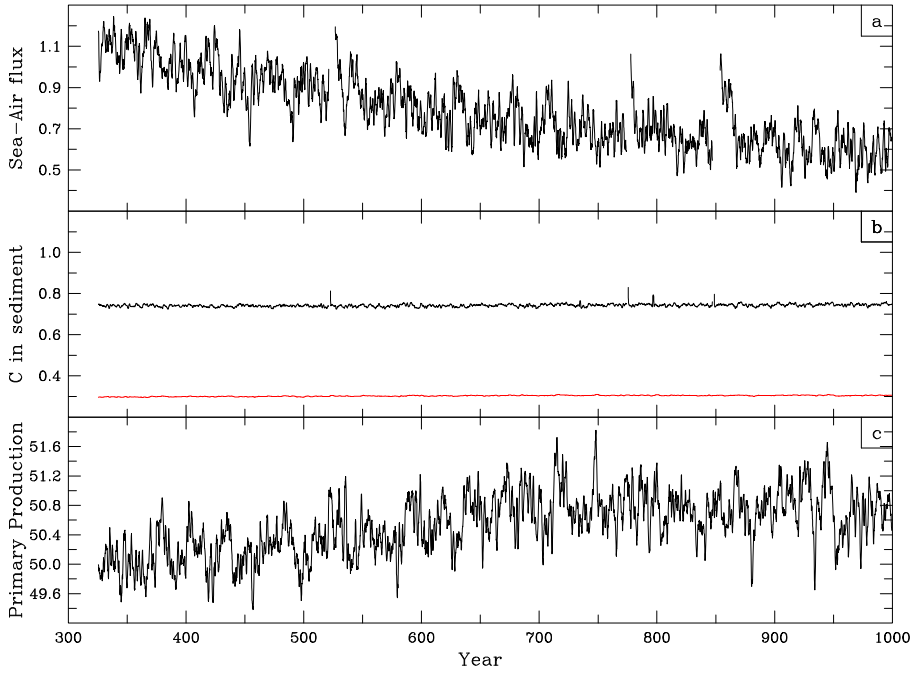

Figure 11. Global **(a)** sea–air flux of carbon dioxide Pg C yr^{-1}, **(b)** carbon content of the organic (black) and calcium carbon sediment (red) pools in Pg C, and **(c)** net primary productivity in Pg C yr^{-1}.

GMDD
8, 8063–8116, 2015

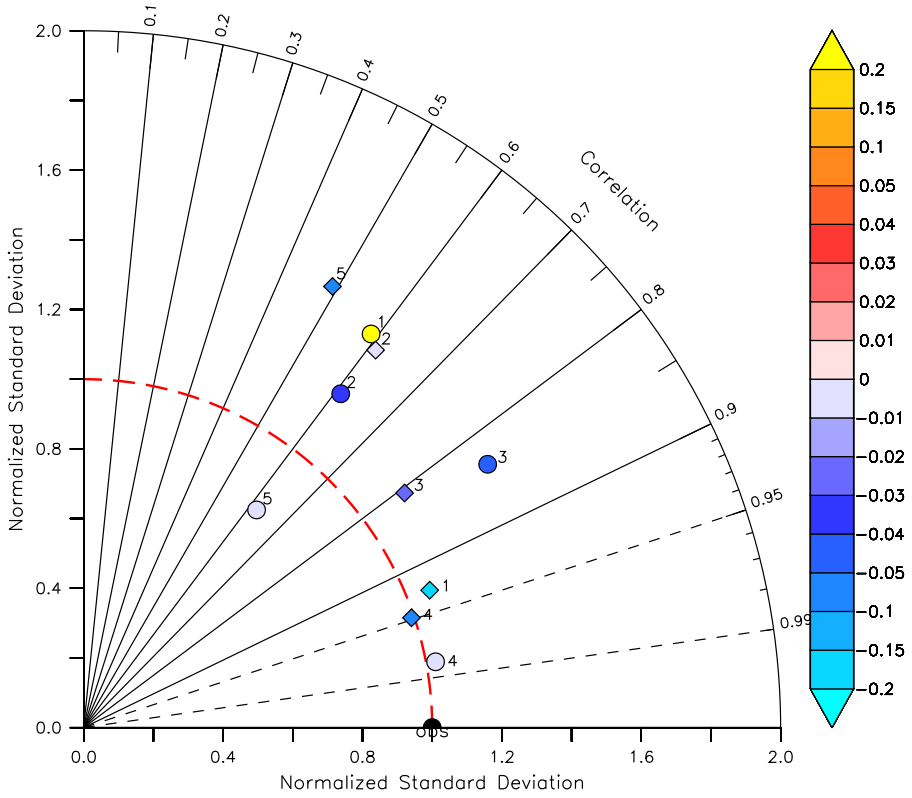

Figure 12. Taylor diagram assessing the response of the ACCESS-ESM1 simulations (circles), and the median of CMIP5 models (diamonds) with observations. The numbers correspond to: (1) Nitrate, (2) Alkalinity, (3) DIC, (4) SST, and (5) (sea surface) Salinity. For explanation please see the text.

GMDD
8, 8063–8116, 2015




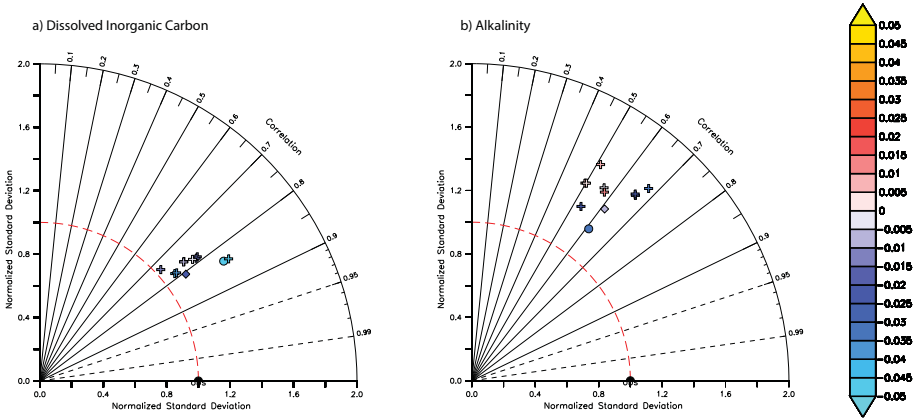

Figure 13. Taylor diagram assessing the DIC **(a)** and alkalinity **(b)** of the ACCESS-ESM1 simulation (circle), the median of CMIP5 models (diamond), and the individual members of the CMIP5 ensemble (crosses) with observations.

GMDD
8, 8063–8116, 2015

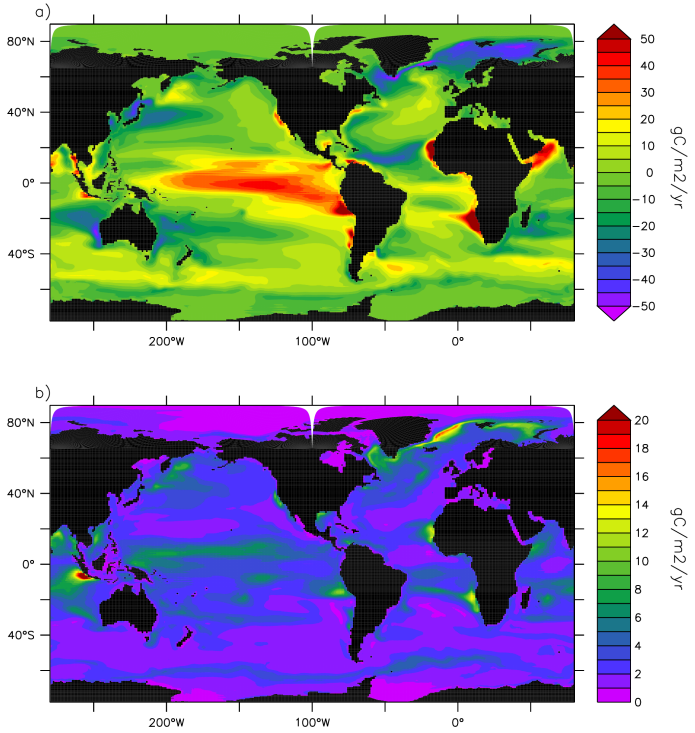

Figure 14. The mean sea–air flux of carbon dioxide for the years 901–1000 **(a)** and the inter-annual variability of sea–air flux of CO_2 defined as the standard deviation of annual fluxes for the years 901–1000 **(b)** in $g C m^{-2} yr^{-1}$.

GMDD
8, 8063–8116, 2015